2024-05-01

Assessing Nordihydroguaiaretic Acid Properties And Its Potential Therapeutic Effect For Glioblastoma

Jose Arturo Guerrero
University of Texas at El Paso

ASSESSING NORDIHYDROGUAIARETIC ACID PROPERTIES AND ITS POTENTIAL THERAPEUTIC EFFECT FOR GLIOBLASTOMA

JOSE A GUERRERO

Doctoral Program in Environmental Science and Engineering

APPROVED:

_____
Felicia S. Manciu, Chair, Ph.D.

_____
Craig E. Tweedie, Ph.D.

_____
Rosa Fitzgerald, PhD.

_____
Marian Manciu, Ph.D.

_____
Stephen Crites, PhD
Dean of the Graduate School

To my

Mother, Isela, and Father, Mario

With love

ASSESSING NORDIHYDROGUAIARETIC ACID THERAPEUTIC EFFECT FOR GLIOBLASTOMA

by

JOSE A GUERRERO

DISSERTATION

Presented to the Faculty of the Graduate School of

The University of Texas at El Paso

in Partial Fulfillment

of the Requirements

for the Degree of

DOCTOR OF PHILOSOPHY

Environmental Science and Engineering
THE UNIVERSITY OF TEXAS AT EL PASO
May 2023

ACKNOWLEDGMENTS

Foremost, I would like to express my deep appreciation to my advisor, Dr. Felica S. Manciu of the Physics Department at The University of Texas at El Paso, for her immense knowledge, encouragement, and most importantly patience and kindness. She has always been supportive and understanding in any aspect of my graduate education and research. Dr. Manciu has always believed in my skill as a student even when I would doubt myself. Her trust in me helped me to be more confident and believe in my abilities.

Besides my advisor, I would like to thank the rest of the thesis committee: Dr. Craig E. Tweedie, Dr. Rosa Fitzgerald, and Dr. Marian Manciu for their support, suggestions, and encouragement.

Finally, I would like to thank my family: my parents Isela and Mario for always believing in me and supporting me in everything. You have worked very hard to allow me to have the opportunity to accomplish my dreams and I will always be grateful for that.

ABSTRACT

This study employs a combination of theoretical and experimental analysis to spectroscopically investigate the biomechanistic structure relationship and therapeutic effects of the Nordihydroguaiaretic Acid (NDGA) chemical derived from the *Larrea Tridentata* plant. These relationships are crucial for understanding NDGA's efficacy in disease prevention, treatment, and potential toxicological effects. While the medicinal and antiviral properties of the NDGA have been studied extensively, there remains a gap in optically identifying and reporting its structural changes. The current research successfully reveals evident trends in NDGA's vibrational signatures, particularly highlighting the absence of the Raman feature at 780 cm^{-1} as indicative of a fully oxidized structural form contributing to its bio-toxicity alongside ortho-quinone accumulation. Additional characteristic signatures of these toxic forms include the Raman lines at 1582 and 1698 cm^{-1} and the IR vibrational line at 1680 cm^{-1}. By elucidating these morphological changes, this study offers valuable insights for the development and implementation of new drugs. Connecting evidence in supporting this statement is the second part of the study, where the NDGA was used for glioblastoma (GBM) treatment. Again, combined experimental Raman and statistical analyses were implemented to detect the drug effect on GBM-treated human cells.

As a potential therapeutic agent, NDGA is a reactive oxygen species (ROS) scavenger and antioxidant. This phenolic lignan had positive effects on multi-organ malignant tumor reduction and inhibition. Although the drug concentrations were beyond the Raman capability limit of their detection, the results show a decrease in altered protein content and ROS-damaged phenylalanine upon NDGA administration. The use of phenylalanine as a biomarker for

differentiating across samples and evaluating NDGA's effectiveness is a new finding discussed here. The creation of lipid droplets and a decline in the altered protein content indicate that treatment with a low dosage of NDGA over long periods reduces abnormal lipid-protein metabolism. The knowledge acquired via this research is significant for comprehending both the positive and negative bio-effects of NDGA as a potential treatment for brain cancer.

TABLE OF CONTENTS

CHAPTER 1
INTRODUCTION

1.1 Traditional Medicine

Traditional medicine (TM) uses beliefs and experience (usually from the use of plants and herbs) to alleviate and/or treat physical and mental diseases. Plants and herbs have been used as medicine by humans for at least 60,000 years, according to fossil records [1]. Early humans faced great difficulty developing treatment from natural products in prehistoric times. A “trial and error” method must have happened with the consumption of poisonous plants that often led to death. However, this approach also contributed to the development of natural medicine from plants and herbs that helped the survival of early humans.

In its various forms and theories, TM, while not perfect, has helped build the foundation of modern medicine known today. The use of botany and herbal medicine as tea originated in ancient China. It is believed that the Chinese emperor Shen Nong drank the first official cup of tea (as a plant infusion) in 2737 BC when a leaf fell into a pot of boiling water [2]. Chinese TM has been recognized consistently as the most advanced, historically and globally. The records of the *Grand Historian (Shi Ji* in Chinese), written by Si Ma Qian (145-87 BCE), a Chinese historian of the Han dynasty, claimed that China's civilization and culture date back five thousand years. However, archaeology has shown that it spans ten thousand years (202 BCE-220) [3]. Today, tea and plant infusion are the second most consumed beverage in the world after water. Tea’s massive system is rich with practical medical technologies and verified experiences that have progressively assimilated into modern medicine.

Tea has become an affordable and effective alternative medicine as the world's population grows older and more individuals suffer from illnesses or bad health. It is mainly

consumed by people who cannot afford or have limited access to health care. TM has been revisited consistently because of its therapeutic effects prior to modern medicine's development. Moreover, several studies have found an inverse relationship between tea drinking and the development of various forms of cancer [2][4][5].

Different cultures have developed beneficial treatments and methods to treat various health diseases. Because Chinese TM gained popularity in western countries, currently, over 1.5 billion people worldwide use TM in addition to or as a substitute for their healthcare [1]. Due to TM's broad reliance on treating diseases, it is essential to investigate the therapeutic and medicinal effects of such practices in more detail. Various forms of tea have already proven to have benefits in promoting optimal health. Drinking tea can support the body's immune system to fight illness more efficiently and may alleviate the severity of the disease [5]. Green tea, one of the most popular forms of tea, is known to aid the host's defense against several diseases by reducing the pathogen's capacity for infection, thus assisting the host's immune system in responding to illness [5]. It can help fight infections and has anti-inflammatory, tissue repair, and improves autoimmune disorders tolerance [5].

The four most prevalent tea varieties on the market are black, oolong, green, and white. These tea and others contain antioxidants, which provide therapeutic effects towards anticancer, cardiovascular, neurological, diabetes, and arthritis, to name a few [4][6]. Based on the many benefits of drinking tea and the fact that modern medicine improves from the investigations of natural products, it is essential to investigate other plants with such properties. In recent years, many studies have focused on a plant known as *Larrea Tridentata* or Creosote Bush and its therapeutic effects. *Larrea Tridentata* is an important medicinal plant of the American-Indians of

the southwest of the US, mainly the Apache [7]. The Apache ate and drank the plant to cure digestive problems and illness [7].

1.2 Larrea Tridentata (la Gobernadora)

The Creosote bush (Zygophyllaceous family), also known as *Larrea Tridentata*, is commonly found in the Mojave, Sonoran, and Chihuahuan deserts, as well as in some parts of Argentina. The drought-tolerant bush is the dominant shrub in this desert, covering thousands of square miles. Locally, it is known as *la Gobernadora*, which means governess in Spanish. Due to its strong scent is referred to as *la Hediondilla,* meaning the smelly little one. The Creosote bush is a 1–3 meter tall, branching, knotty evergreen shrub, as represented in Figure 1.1. The leaves are opposite and have two asymmetrical leaflets about 1 cm long. [8] The plant's leaves have been used in traditional medical practices in tea infusion for generations to treat and prevent more than 50 diseases.[8]

Figure 1.1. *Larrea Tridentata* bush and the plant's flowers. [9][10]

Tea has long been used in Mexico to remedy kidney and gallbladder stones, which continues even today in areas where the plant grows abundantly [6]. The plant has many benefits

when taken as herbal medicine, including treating renal disease, tuberculosis, gallbladder ailments, rheumatism, diabetes, skin disorders, cardiovascular disorders, neurological, and cancer [8]. Modern medicine continues to advance and depart from traditional medicine. However, TM is still a strong foundation for critical and scientific understanding of many drugs' efficacies and for studying various bio-mechanisms.

The known beneficial qualities of *Larrea Tridentata* fade if consumed in high concentrations, leading to hepatotoxicity. This was one of the main motivations and the reason for its banning in 1970 by the US Food and Drug Administration (FDA) of the United States and discouragement of its employment in treatments or as a food ingredient. Despite the FDA prohibition, studies were still being conducted to scientifically understand its benefits for future therapeutic usage. Examples include research assessing the safety of a low-dose therapy to participants who previously used the plant for traditional purposes, from oral to topical applications [11]. The results showed that patients with no history of prior liver illness did not develop them because of the usage of *Larrea Tridentata*; either in a complex herbal combination comprising less than 10% tincture or in an oil extract for topical treatment. Based on these investigations, a correlation between the concentration of *Larrea* and its toxicity was demonstrated. Also, it had been suggested and recommended less usage of *Larrea Tridentata* capsules, as it can lead easily to a harmful overdose. This remark could also be regarded as a consequence of a poorly understood metabolic effect of all plant components [11].

Creosote bush is well recognized in the natural product chemistry as a main producer of nordihydroguaiaretic acid (NDGA), a lignan deposited on the plant's leaves (at their surfaces). The NDGA is responsible for most of the plant's therapeutic effects. Thus, its successful extraction and purification contributed to the elimination of other toxic plant components,

reducing the potentially harmful influence of direct consumption of natural products. Consequently, NDGA's detailed structural forms will be the focus of the first part of this study.

1.3 Nordihydroguaiaretic Acid (NDGA)

The primary extract of the Creosote bush, NDGA, is a phenolic lignan with antioxidant properties and ability to scavenge reactive oxygen species (ROS). It was scientifically identified and extracted from the plant in 1945 and purified chemically in 1955 [12][13]. Direct evidence supporting that NDGA is the main component of the plant is shown in Figure 1.2, where the two spectroscopic spectra of the NDGA and the plant infusion are presented [14]. In addition to much broader bands in the spectrum of the plant infusion, which are attributed to OH vibrational components from water, there is an obvious similarity between these spectra.

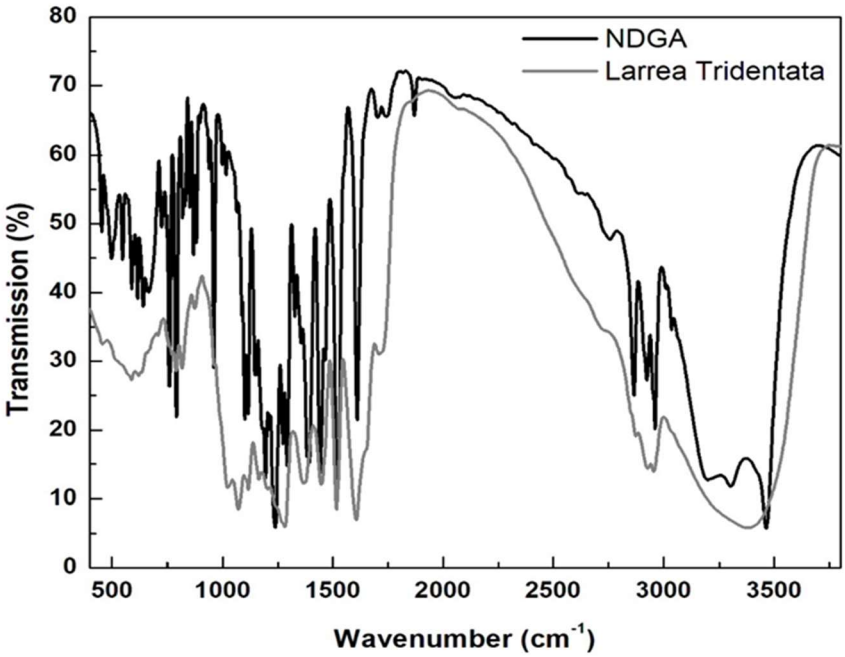

Figure 1.2. Infrared spectra of NDGA and *Larrea Tridentata*[14].

As seen in Figure 1.3, NDGA's molecular structure contains four phenolic hydroxyl groups, allowing for scavenging ROS. Examples of ROS are hydroxyl radicals, superoxide anion, singlet oxygen, peroxonitrite, and hydrogen peroxide. The antioxidant makes up about ten percent of the dry weight of *Larrea Tridentata's* leaves and eighty percent of all flavonoids and lignans present in the plant's resin [11].

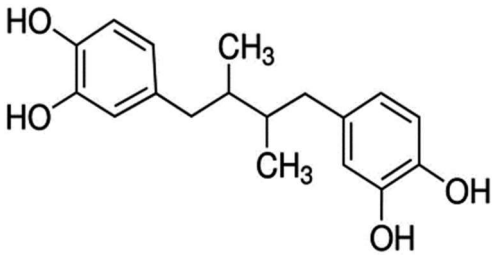

Figure 1.3. Chemical structure representation of Nordihydroguaiaretic acid (NDGA) in neutral form.

ROS, also known as free radicals, form and accumulate in enormous quantities in living organisms. These quantities can cause damage to cells due to the oxidative stress processes. Free radicals enter the body in many forms, from air/water pollution and from processed foods. Given that oxidative stress and inflammation are critical pathogenic causes of many renal diseases, NDGA has emerged as a potential option and remedy because of its significant importance as an antioxidant and ROS scavenger. In addition, NDGA has anti-tumorigenic and anti-proliferative properties for suppressing tumor growth by inhibiting metabolic enzymes and receptor tyrosine kinases (RTK) phosphorylation [15]. The chemical structure of NDGA changes due to the oxidation of its phenolic hydroxyl groups creating different morphologies. The ability to discriminate between unoxidized and oxidized NDGA forms is valuable for understanding the compound's therapeutically benefic effects. Such known structural modifications could increase the compound's therapeutic potency and reduce its toxic effects. While NDGA treatment at more than 100 mg/kg for extended periods is harmful, a high dose over a short period (bolus therapy)

may have some favorable chemotherapeutic effects. This later approach should be also considered and further investigated [16].

However, an accurate distinction between such morphological changes of NDGA has yet to be optically detected and studied. The lack of optical studies of NDGA is due to the compound needing to be optically inactive in its natural form. However, a decreased fluorescence intensity from NDGA binding with fluorophores in proteins is reported when administered as a drug [17]. It has been theoretically predicted that NDGA absorption happens at about 280 nanometers (nm) in the UV-VIS spectrum [18]. In this case, it was not a direct identification of NDGA itself but of its association with significant carrier proteins such as serum albumins. This finding was essential for understanding the transport and metabolism of NDGA as a drug [17]. However, other chemical conformations of NDGA associated with oxidation or binding to analytes have absorption in the same UV-VIS optical region [18]. Therefore, more research on the distinction between NDGA morphological forms is needed to understand the drug's toxicity, potential harm to the body, and any positive benefits. Raman Spectroscopy and Fourier Transform Infrared Spectroscopy (FTIR) are optical techniques that enable a label-free detection of these morphological changes of NDGA.

In recent years, NDGA and its derivatives have been gaining interest as a chemotherapeutic agent against cancers, specifically for brain cancer, which is the main objective of the second part of this study. Other lignans have also succeeded as pharmaceutical compounds and have shown promise in cancer treatment [19]. In the rodent model, NDGA has a lipoxygenase (LOX) inhibitory effect and the ability to enhance fatty acid oxidation via peroxisome proliferator-activated receptor α (PPARα)-dependent pathways that suppress tumor growth [20]. The LOX inhibitory effect depends on the cancer cell type and context. Several

cancer cells have altered LOX properties and protein and lipid alteration. Prior to investigating NDGA's anti-tumor properties, we first need to be able to identify and discriminate optically between beneficial or detrimental morphological forms of NDGA.

1.4 Glioblastoma

Cancer treatments are limited to surgery, chemotherapy, and temozolomide to shrink administration to shrink tumors. Even though the death rate from cancer has been steadily decreasing in the United States since 1990, cancer remains a serious hazard to human health [21]. Another difficulty in effectively treating cancer is that when a tumor grows in multiple organs, it might take on distinct phenotypes, which can alter cancer progression and make it challenging to avoid metastasis [22][23][24]. The spread of cancer to other organs further complicates treatment. The most effective therapies should target organ-specific malignant tumors and mediate multi-organ metastasis. Typically, neoplasm and metastasis cancer cells migrate from other organs through the bloodstream. However, brain tumors in the central nervous system are formed intracranial. The most common malignant glioma is the intracranial glioblastoma multiforme (GBM) analyzed in this work.

Detection and diagnosis methods include Magnetic Resonance Imaging (MRI), Positron Emission Tomography (PET), Computed Tomography (CT), and Ultrasound Sonography (US). Due to GBM growing with tendrils that are too small to detect, the removal of the main tumor by surgery is usually not enough. Despite recent improvements in cancer therapies, understanding the different routes and processes that lead to cancer occurrence, resistance, and recurrence remains a problem. Again, using Raman microscopy, which is an optical technique with all the advantages of optical methods for real-time diagnosis, additional important insights are now

achievable. Raman also has the significant advantage of not requiring fluorescent tagging for identifying molecular signatures. Consequently, has recently gained popularity [25]. It has been proven that Raman methods have the ability to detect brain cancer cells in humans with higher accuracy than MRI [25].

It is essential in research to investigate innovative ways of treatment against brain cancer and to improve the treatments available. Based on the studies of NDGA, the antioxidant possesses excellent promise as a treatment not just for glioblastoma but also for several other cancer cell lines. In vitro, NDGA exhibits anti-tumor effects in various cancer cell lines in concentrations ranging from 1-100 μm [19]. In animal models with tumors, NDGA tested in doses of .750-100 mg per kilogram of body weight held good promise [26]. However, it is essential to consider both the toxic effects of NDGA in high concentrations and the reported 5-lipoxygenase (LOX) inhibition by NDGA. In the rodent model, NDGA is known to have lipoxygenase (LOX) inhibition effects [20]. This inhibition is an essential characteristic of NDGA for elevated levels of 5- LOX and 12-LOX, which promote tumor cells' growth and pro-survival factors as they regulate pro-inflammatory responses [27]. LOX causes lipid-peroxidizing enzymes that alter lipid content and, if over-expressed, can develop cancer due to high levels of cell stress [19][28][29]. Understanding the beneficial effects of the 12- and 5-LOX inhibition by an antioxidant such as NDGA is important because it can target critical pathological pathways simultaneously in proliferation, deficient apoptosis, metastasis, cancer angiogenesis, chronically elevated oxidative stress, as well as in the Niche of the tumor [19].

To this end, Raman spectroscopy is a powerful and effective label-free technique for analyzing and discriminating between normal cells and tumor cell lines. The ratio between lipids and proteins in the Raman spectra could determine the cancer grade. It also can differentiate

between several types of brain cancer, including glioblastomas, meningiomas, and metastatic tumors [30]

Preclinical and clinical data showed that some of the recently developed NDGA analogs have great potential as cancer therapy, alone or in conjunction with other drugs. In the past 60 years, preclinical trials in cell culture and mice have shown that the lignan NDGA is a promising medication for the prevention or treatment of various diseases and cancer types [19]. However, there has yet to be much success in translating these findings into a therapeutic setting. Improving our understanding of their mechanisms of action and avoiding unwanted toxicological effects are critical to transforming TM into practice. Thus, in this study, we will first identify and discriminate the morphological form of NDGA using Raman and FTIR spectroscopy. This information on Raman and IR signatures of NDGA is essential to have before investigating the anti-tumor effects of NDGA in glioblastoma, as it allows for a better understanding of the compound's influence.

CHAPTER 2

EXPERIMENTAL BACKGROUND AND METHODOLOGY

2.1 Spectroscopic Techniques

Spectroscopy is a branch of science used to investigate and measure spectra produced when matter interacts with or emits electromagnetic radiation (i.e., electrons, protons, and ions). as a function of collision energy. In optical spectroscopy, the incident light radiation (from a broad lamp source or a monochromatic laser) when interacting with the atoms/molecules in a sample is partially absorbed or radiated by scattering. The occurring changes in frequencies between the incoming and outgoing radiation contribute to identifying any material. They are considered a “fingerprint” for particular molecules since no two types of molecules vibrate the same. Spectroscopic methods are based on emission, absorption, fluorescence, and scattering phenomena that can be used to obtain a qualitative and relative quantitative analysis of materials [31]. Sensitivity, safety, noninvasiveness, miniaturization, low operating costs, and quick, automated sample turnover are some benefits of spectroscopic analytical methods.

The qualitative analysis establishes the identity of constituents in the sample, while the relative quantitative analysis estimates the relative concentration of a constituent/chemical substance in the studied sample. The energetic modifications of the molecules are made of translational, rotational, vibrational, and partly electrical types. These are related to the degrees of freedom in the chemical sample's bonds, which can change as the molecules interact with a monochromatic laser (in the case of Raman spectroscopy) or with the light from a broad lamp source (in the case of infrared absorption). The electromagnetic energy of the light (with a dominance of the electrical type of energy) gives rise to absorption and emission in the

ultraviolet and visible regions of the spectrum. In addition to absorption, most of the scattered radiation is elastically scattered, having the same frequency as the incident radiation. This radiation is called Rayleigh scattering. Only a tiny amount of the radiation has a different frequency than that of the incident radiation. This radiation amount constitutes the Raman scattering/effect, which is employed in current data collection.

No change in the wavelength of the individual photons occurs in Rayleigh scattering, which does not give any information about the sample. Spectroscopic techniques such as Raman and Fourier transform infrared (FTIR) absorption can be used together to study the molecules' composition in samples. Fourier spectroscopy is a common term that describes the analysis of varying signals into their constituent frequency components. Mathematical approaches named after J.B.J. Fourier are potent in spectroscopy and have been discussed in detail elsewhere [31]. Fourier transform can be applied to various research fields like infrared absorption, Raman, nuclear magnetic resonance (NMR), and electron spin resonance (ESR).

2.2 Raman Spectroscopy

Raman spectroscopy, one of the techniques employed in the current study, is named after its inventor Sir Chandrasekhara Venkata Raman, an Indian Physicist. He discovered that the interaction of incident radiation with a molecule could produce radiation with different frequencies. Raman spectroscopy is a technique based on the Raman effect or the inelastic scattering (Raman scattering). It is used in the scientific investigations and analyses of materials to provide additional chemical and structural information about various molecules.

The samples are illuminated with an intense monochromatic laser source, the incident radiation. The interaction occurring with the constituent molecules of the sample produces the

scattering radiation, which is collected using a spectrometer or CCD camera and further analyzed. When the incident radiation has a higher energetic (frequency) value than the scattered radiation, Stokes frequency lines appear in the Raman spectrum. Anti-Stokes lines appear when the incident frequency is lower than the scattered radiation. These Stokes and anti-Stokes vibrations are either above or below the Rayleigh scattering line, which happens when the radiated frequency matches the initial one, as illustrated in Figure 2.1.

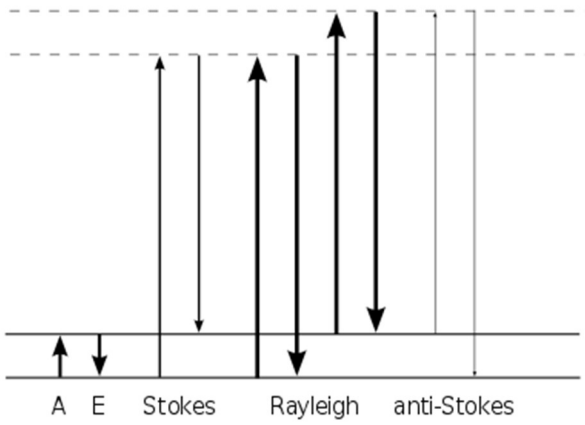

Figure 2.1: Raman stokes, anti-stokes, and Rayleigh scattering processes via virtual states (denoted by dash lines). Absorption A and emission E are between real energy levels on the left. [32]

This Stokes terminology arose from the Stokes' law of fluorescence, which stated that a fluorescent radiation always occurs at lower frequencies than the exciting radiation [33]. A pure rotation usually gives a spectrum in the microwave region or far infrared. Other types of molecular vibrations provide a spectrum within most of the infrared spectral region. The significant difference between fluorescence and Raman scattering is that the latter effect can happen for any frequency of incident radiation; it is not always a resonant effect. In practice, the fluorescence effect is anchored at specific frequencies only. On the other hand, Raman scattering has a constant separation from the excitation frequency. The polarization needs to change during

molecule vibration to obtain a Raman spectrum. Also, avoiding fluorescence in the sample is vital since it is much stronger than the Raman scattering, interfering with the gathered results.

The Raman effect is weak, typically 10^{-8} of the intensity of the incident, exciting radiation. The classical approach of the Raman effect considers the scattering of molecules as a collection of atoms undergoing simple harmonic oscillations, following appropriate quantization of the vibrational energy [34]. Electromagnetic radiation can be defined by its wavelength λ, frequency ν, and wavenumber ṽ. They are interconnected as seen in equation 2.1. The wavenumber is measured in cm^{-1} (inverse length), the number of waves in one wave train.

$$\tilde{\nu} = \frac{\nu}{c} \qquad \tilde{\nu} = \frac{1}{\lambda} \tag{2.1}$$

where c = 2.99792458x10^{10} cm/s is the speed of light, v is the frequency in the cycles per second or Hertz, and λ is the wavelength in cm. While wavelength is a radiation property, energies and frequencies unite the radiation with molecules.

In quantum theory, the energy of the photon, E_p, is given by equation 2.2:

$$E = h\nu \qquad E = hc\bar{\nu} \tag{2.2}$$

where h=6.6256x10^{-27} erg-sec is the Plank's constant.

The molecule's rotational, vibrational, or electrical energy changes due to energy conservation when a photon is emitted or absorbed. The energies are positive if absorbed and negative when lost. The radiation causes an induced dipole moment in the sample, which is related to the polarizability α, the dipole moment P, and the electric field E by:

$$P=\alpha E \tag{2.3}$$

The dipole moment is a vector and polarizability a tensor. The polarizability measures the distortion of the molecule's electron cloud caused by the electric field. This change in the electron cloud allows for optical frequencies to undergo amplitude changes in the oscillations of

the dipole moment, resulting in measurable Raman frequency components. A Raman spectrum is a plot of Raman scattering intensities as a function of the change in frequency from the incident frequency; the so called Raman shift.

Since most of the samples are measured at room temperature or in thermodynamic equilibrium, the molecules are in their ground states. The energy of the incident radiation is completely absorbed, causing the molecules to be excited. The emission energy of the scattered light can be the same as that of the incident radiation (elastic scattering) or at different frequencies (Stokes and anti-Stokes). At room temperature, the Stokes lines are more intense than the anti-Stokes lines. This effect can be used to examine the sample as their ratio depends on temperature [30].

Concerning temperature-dependent Raman measurements, both Stokes and anti-Stokes scattering lines can be used; the ratio of the intensities of the same Raman peak in both regions is frequently calculated for determining the purity of materials or structural changes [35]. However, the Stokes lines are employed mostly to determine the sample's chemical structure due to their stronger intensities.

2.3 Fourier-Transform Infrared Spectroscopy

Fourier-transform interferometry was initiated in the late 1880s, when Albert A. Michelson invented the interferometer known today as the *Michelson interferometer*. The instrument was well received at the time, awarding Michelson the 1907 Noble Prize in physics. He and Morley used this very instrument to perform a well-known experiment to determine the speed of light [36]. Fourier-transform infrared spectroscopy (FTIR) is used to measure infrared radiation as a function of both wavelength and frequency to determine the functional groups in a

compound. When an object is exposed to the infrared radiation, part of the radiation is absorbed by the object, and some of it goes through (is transmitted). Because molecules are made up of numerous groups of atoms rather than simply a two-atom pair, each of these atomic groups has its vibrational transitions and influences the energy of the vibrational changes of the other groups in the molecule [37]. Thus, the resulting signal at the detector represents a "fingerprint" spectrum that is unique to the sample, as seen in Figure 2.2.

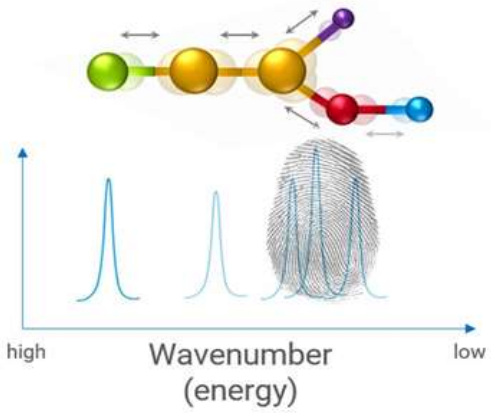

Figure 2.2: Infrared (IR) spectra produced by bands of various functional groups viewed as the sample's unique fingerprint. [38]

FTIR can also indirectly determine the electric properties of samples, such as deciding whether it is an insulator, superconductor, or semiconductor, as well as band gaps due to the change of the electric dipole moment. FTIR spectrometers became more common because of their speed, accuracy, and sensitivity, which were previously impossible to measure with wavelength dispersive spectrometers. Infrared radiation is an invisible electromagnetic radiation just below the red spectral region in the visible spectrum, with a wavelength range from 700 nm to 1 mm [37]. Concerning the interaction of this type of radiation with the matter, a dominance of transverse vibrational transitions happen. Infrared radiation is too low to affect the electrons within the individual atoms and too powerful for translational shifts [37].

In the vibrational transitions, the absorbed incident radiation by the sample can be explained in terms of resonance conditions, where the incident radiation frequency matches the natural frequency of the normal modes of the molecules. The best way to describe this effect classically is by describing the modes between the atoms as weightless springs obeying equation 2.4 also known as Hooke's law:

$$F = -kx. \tag{2.4}$$

The potential energy of a molecule obeying Hooke's law is obtained by integrating the equation of the force:

$$F = -(dV/dx) \qquad V(x) = \frac{1}{2}kx^2 \tag{2.5}$$

Graphically, the potential in equation 2.5 is a parabola. It is referred to as a harmonic potential because the molecule performs a harmonic motion [39]. For infrared absorption to occur there must be a change in the dipole moment of the vibrating molecules.

The acquired signal is composed of the normalized absorption and/or transmission to the response of the detector. When added together, the absorption and transmission become a quantity of one. As seen in equation 2.6 this can be expressed as a ratio for the transmitted intensity I_T to the initial intensity I_I, modulated by the thickness, d, of the sample and the coefficient of absorption α , which is specific to the material. The relationship between the transmitted and incident at specific wavenumbers v is called the Bouguer-Lambert-Beer Law of absorption of light.

$$T=\frac{I_T}{I_0} = e^{-\alpha d} \tag{2.6}$$

Light can also be reflected, $I_R(v)$, in certain materials. Although the contribution of such intensity is incredibly low and depends on the material type, it is provided by:

$$I_I(v) = I_0(v) - I_R(v) \tag{2.7}$$

2.4. Advantages and Disadvantages of Raman and FTIR Techniques

A main advantage of these spectroscopic techniques is providing the structural characterizations of organic and inorganic materials at the molecular level in a label-free manner. However, as with any technique, they also have their limitations.

For example, when the fluorescence of some reflective materials is hiding entirely or part of the Raman vibrations, some other approaches that decrease the fluorescence are used. One approach is lowering the excitation wavelength, so the Raman peak is shifted to a lower wavelength. Photo-bleaching is another approach, where the sample is irradiated for a period of time, breaking down the fluorescent molecules and reducing the fluorescent background. Photo-bleaching should be approached with caution if dealing with biological samples as it can create irreversible damage. Since fluorescence is a limitation in Raman spectroscopic measurements, which does not hamper infrared types of investigations based on FTIR, complementary analysis is needed for an improved characterization.

While fluorescence /photoluminescence can diminish the signal in the Raman spectroscopy, even overwhelming it, in a non-dispersive technique such as FTIR, the incoming radiation frequencies are not spatially separated. The sample's signal is compared to a signal coming from a moving mirror, as will be described below in the experimental set-up section. When the natural frequency and wavelength of the sample match, it increases/enhances the wave properties and signal.

On the other hand, FTIR spectroscopic method is sensitive to water absorption, making it inappropriate for studying aqueous materials. For the measurement of aqueous solutions, because water produces weak scattering in the visible range, Raman measurements are more suitable.

Because both methods have their advantages and limitations, they are typically used together to complement each other in providing different properties of the sample.

2.5 Experimental Set-Up – Alpha 300RAS Witec Confocal Raman System

The main goal of any analytical technique is to obtain the best results. With basic Raman spectroscopy, it is possible to get a good signal from a location on the sample, record it using a spectrometer or a multi-channel detector, and disperse it to a spectrum. This is assuming the sample emits minimal fluorescence, which does not hide the signal. Examples of Raman spectra, with labeled assigned functional group are presented in Figure 2.3.

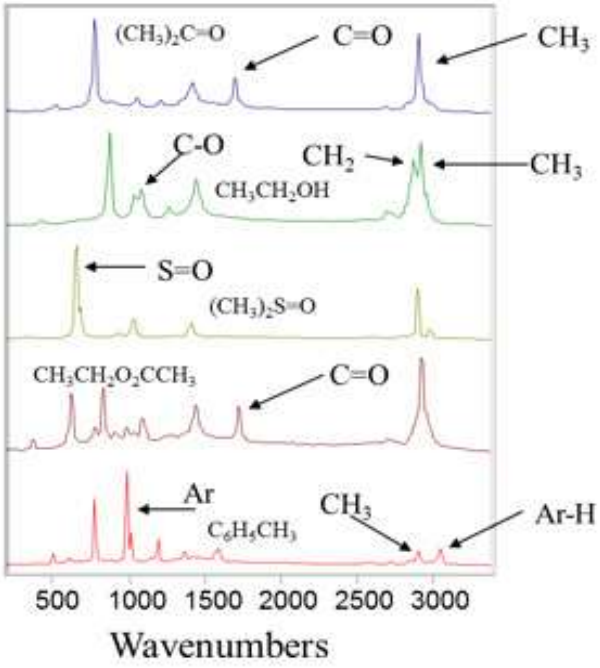

Figure 2.3: With peaks from certain functional groups indicated, below is an example of five molecules: acetone, ethanol, dimethyl sulfoxide, and ethyl acetate and toluene respectively.[40]

Raman spectrophotometers can be non-dispersive or dispersive. Raman spectra are recorded over a range of 4000-10 cm^{-1}. In organic molecules, the Raman active normal modes

usually occur in the 4000-400 cm^{-1} [41]. Overtones, combinations, and difference bands are rare in the Raman spectrum, making it significantly more straightforward than its infrared (IR) counterparts.

Measurements are more easily accomplished using Raman spectroscopy than other methods, mainly because of a less demanding sample preparation. However, basic Raman spectroscopy does not give a controlled sampling volume. Thus, over the years, another technique, Raman microscopy, has been developed on the foundation of Raman spectroscopy and confocal microscopy. In confocal Raman microscopy, the desired amount of the sample can be analyzed with a high precision laterally (on the x-axis and y-axis), as well as in depth (on the z-axis). The depth profile type of sample analysis is enabled by the addition of a confocal pinhole as part of the experimental setup. It is a defining feature of confocal Raman microscopy.

A schematic of the optical pathway of the confocal Raman microscope is shown in Figure 2.4.

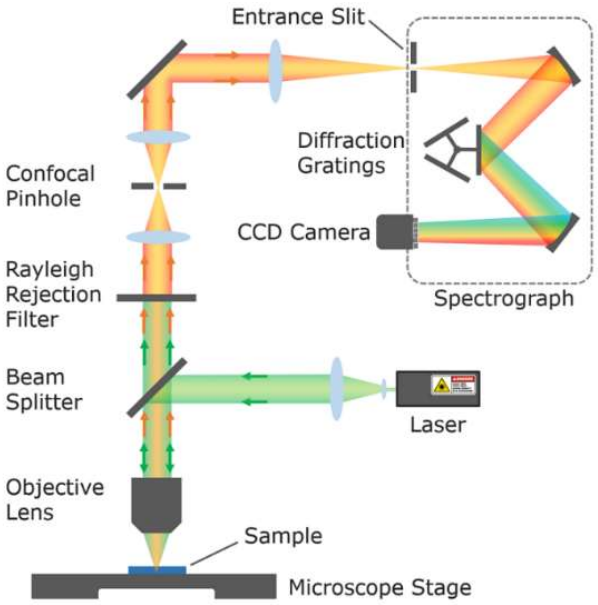

Figure 2.4: Schematic optical layout of a Confocal Raman Microscope with assigned labels for each component of the system. [42]

Numerous fundamental parts make up a basic Raman system: a laser, objective lens, rejection filter, spectrometer, and detector/CCD camera. Employment of an optical microscope in a confocal Raman system allows for visual and spectroscopic exploration, such as a single point, mapping, or imaging measurements. The scope of the objective lens is to collect the electromagnetic radiation emitted from the targeted spot with a laser and send it to a monochromator, which will transmit only a mechanically selectable narrow band of wavelengths or radiation from a range of wavelengths available at the input. The microscope will enable the examination of each point at a time by measuring the scattered and absorbed radiation from a particular location in the sample.

Historically, the 435.8 nm excitation line of coiled low-pressure mercury arc lamp was used as a light source until the 1960s [41]. Laser sources became available later and replaced the mercury lamp, as they provided a more stable and intense beam of monochromatic radiation [41]. From a variety of laser sources, the one using a 532 nm excitation wavelength became popular, because it provided a relatively high Raman excitation energy with little fluorescence. However, soon it had been realized that longer wavelength lasers, such as those with a wavelength of 785 nm, 830nm, and 1064 nm, induce less electronic excitation. Currently, such laser sources are utilized frequently for an even higher reduction in fluorescence [41].

The objective lens collects Rayleigh and Raman scattering from the sample, which is then transmitted through the beam splitter toward the Rayleigh rejection filter [42]. As mentioned before, only about 1 in 10 million of the photons are Raman scatter; the rest are Rayleigh scatter and contain no information about the sample. The purpose of the filter is to remove the Rayleigh scattering and Raman scattering to remain. The rejection filter can be either an edge or notch rejection filter. Edge filters are precise long-pass optical filters that transmit all wavelengths past

their "edge" after absorbing all wavelengths up to that point. They allow only a certain scatter to pass [42]. Notch filters are holographic filters having a sharp absorption peak at one specific wavelength, designed to coincide with the laser wavelength, and transmit all desired wavelengths [42].

The Raman scatter then travels to a confocal pinhole that is utilized to focus the residual Raman scatter, improve the spatial resolution, and reduce the fluorescence background of the Raman mapping. As seen in Figure 2.4 the pinhole is located between two converging lenses. The focused Raman scatter is then allowed to pass through the spectrograph, where is separated by wavelength, and recorded by an array detector [42]. The spectrum generated allows for the identification of various functional groups in a sample.

Clear advantages of confocal Raman microscopy usage were acknowledged in many fields of nanoscience, material science, and nanotechnology. Another rapidly growing application of confocal Raman is in the bio-science arena and pharmaceutical industry. The ability to give improved spatial resolution allows us to examine cells in their natural environment. Little sample preparation is needed for such measurements, making confocal Raman unique. Concerning bio-pharmaceutical applications of the technique, the resolution allows further investigation of the chemical changes in the structure of individual cells, spectroscopically and microscopically. The sample imaging that can be generated through confocal Raman mapping enables visualization as well. Mapping can be performed in two ways: by scanning the light beam throughout the sample or by moving the sample using the three-dimensional x-y-z axis scanning stage. Furthermore, a complete spectral information at each pixel can be extracted from such image, allowing us to see the Raman signature of components within the cell.

Thus, with quality confocal Raman microscopy, it is possible to analyze individual particles in dimensions of 1µm. In dispersive instruments, a notch filter, and a quality grating monochromator, called a bandpass filter, are used to isolate a single laser beam. These monochromators are used to separate relatively weak Raman lines from intense Rayleigh scattering radiation. For an increase resolution, double or triple grating monochromators, rejection filters, super notch filters, holographic notch or edger filters, and holographic filters are used [41]. The laser gives a visual inspection of the sample covering an area of about 1x1x5µm. A significant advantage of Raman spectroscopy is the high resolution that can be obtained compared to FTIR, which is about ten µms. The confocal Raman microscopy, a valuable techniques in biochemical research, was used in this study. Also, a high resolution/super-resolution was maintained throughout the experiments.

The system employed in this study is the *alpha 300RAS Witec* confocal Raman system located in the Optical Spectroscopy and Microscopy laboratory at the University of Texas at El Paso. This system is showed in Figure 2.5.

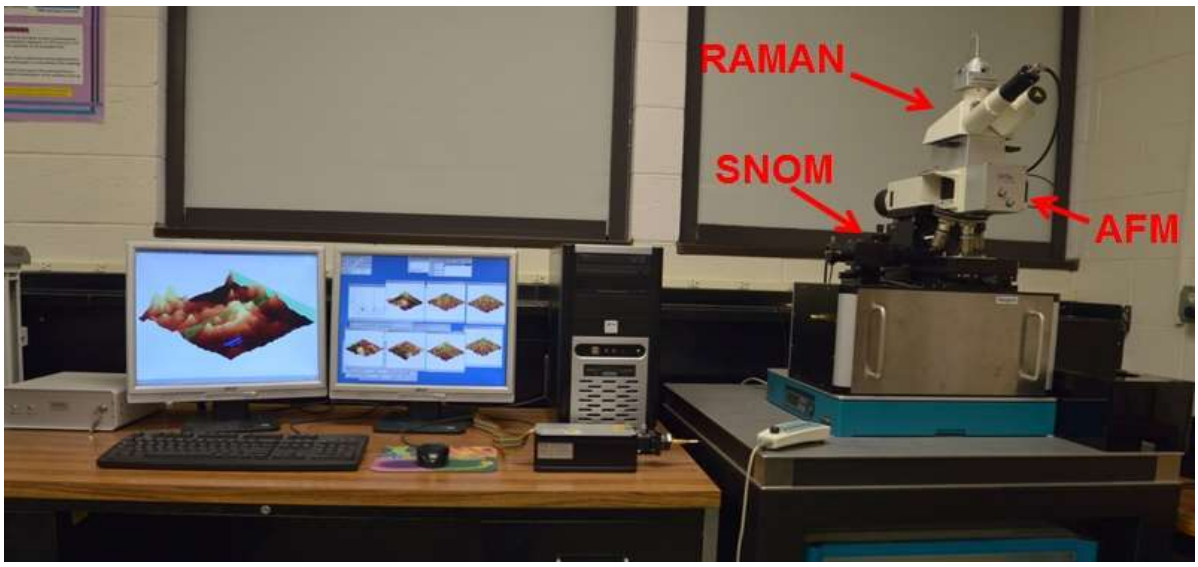

Figure 2.5: The 300RAS Alpha Witec confocal Raman system located in the Optical Spectroscopy and Microscopy laboratory and employed for this study.

2.6 Experimental Set-up - Bruker IFS 66v FTIR System

Several subsystems are involved in Fourier transform infrared measurements, namely emission sources (lamp source), collection devices (detectors), modulation (mirrors and beamsplitter), and transformation; the last two are usually software controlled. In using a conventional spectrometer, which consists on dispersive elements like prism and grating, there is a need to scan across a single line/wavelength in the spectrum. When Fourier concepts are applied to optical spectroscopy, enables a new technology (i.e., interferometry) to give the entire spectrum at once [36]. In Fourier transform spectrometry, the purpose of the interferometer is to measure the intensity of each wavelength emitted from the light source. While the whole FTIR system is quite complex, as can be seen in Figure 2.6, the interferometer is the most vital component; thus, it is "its heart".

The computer oversees controlling optical components (automatically moving mirrors to redirect the light beam to different detectors), collecting, and storing data to conduct further calculations that have as the final product, the spectra. Because of interfacing the interferometer with the computer, spectra can be arithmetically manipulated in many ways. For example, interfering absorbance can be eliminated by subtracting from composite spectra the absorption bands due to interfering components [36].

An FTIR interferometer is built on the *Michelson interferometer* principles of operation and concepts that were explained previously. As shown in Figure 2.7, where the optical path inside an interferometer is presented schematically, it has also several components. One vital component is a lamp source (light source) that emits radiation/light that is detected to a collimator, and next to a beamsplitter. Another essential part is its two modulating mirrors, one moving (labeled in Figure 2.7 "Mirror Scanner") and one stationery.

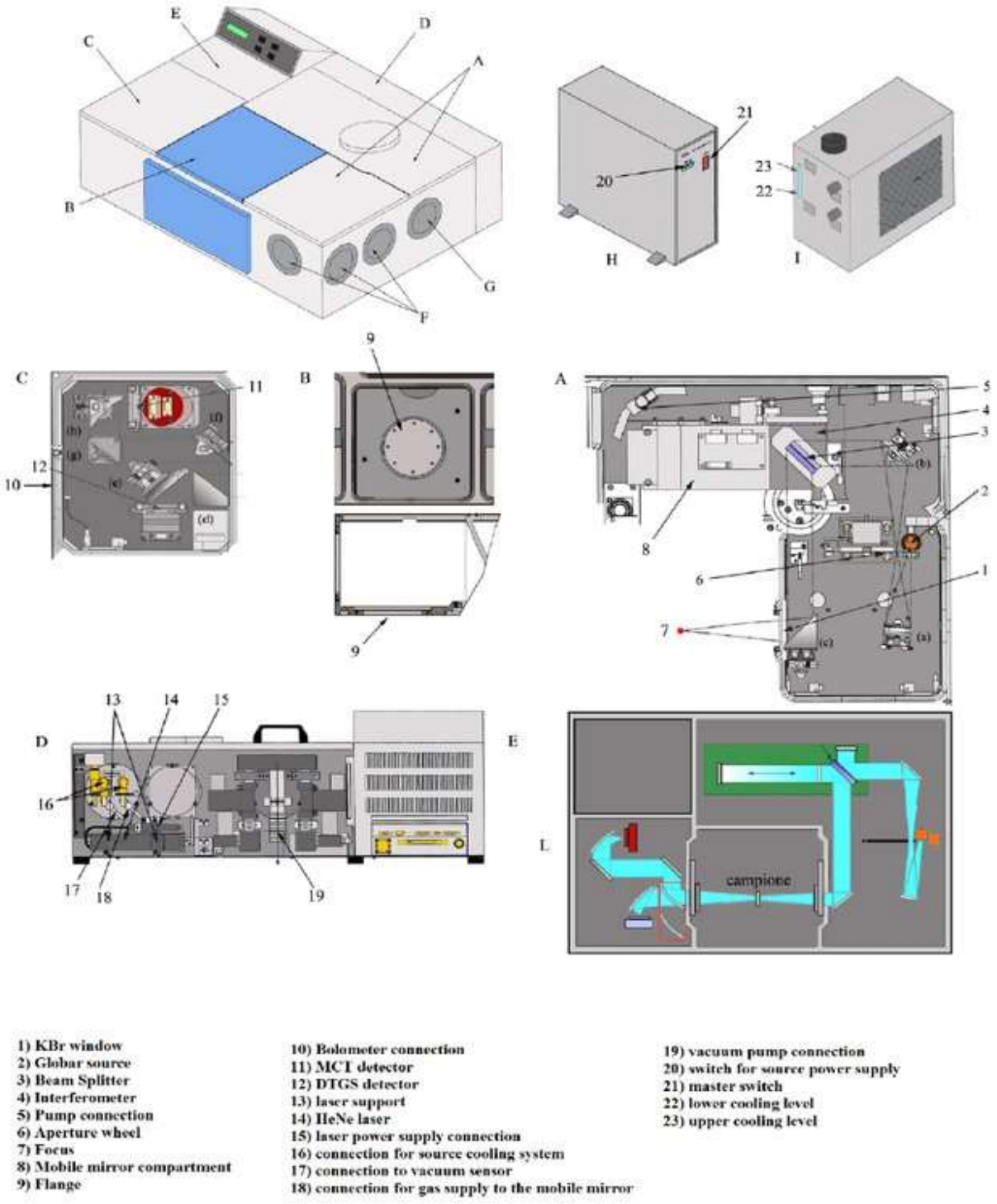

Figure 2.6. An illustration of the Bruker IFS 66v FTIR system (Bruker Optics Inc., Billerica, MA) general layout and information on its individual parts. Compartments for the Michelson interferometer (A), sample chamber (B), detectors (C), and optical systems (L).[43]

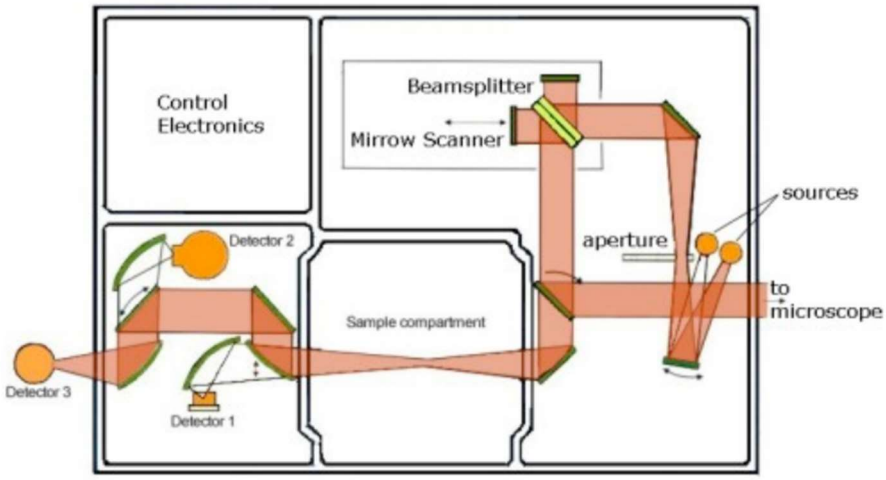

Figure 2.7: Bruker IFS 66v FTIR system optical path.[44]

The two plane mirrors are conjointly perpendicular; one mirror is allowed to move along the axis perpendicular to the other mirror. As illustrated in Figure 2.7 a beamsplitter is placed between these mirrors, allowing half of the light to be reflected and the other half to be transmitted. The beam-splitter is oriented 45 degrees from the incoming infrared radiation/light and divides it into two beams of light of equal intensities [37].

The generated signal is called an interferogram, which is a recording by the infrared detectors of the modulated intensity at the beamsplitter. The two split beams of light that undergo two optical paths create the interference pattern. They are reflected by the mirrors back to the beamsplitter, where they recombined. Thus, the signal is captured as a function of the path difference between the interferometer's two optical paths. A Fourier transformation is also conducted to obtain the final spectrum. The basic integral equation used in this data processing can be obtained from the definition of the Fourier integral theorem and the principle of superposition of waves [36].

When the two beams recombine, two scenarios can happen. The light beams, which are electromagnetic waves, can undergo constructive or deconstructive interference. The interference depends on the electromagnetic waves' optical path difference and wavelength. The optical path has a difference of 2x, called the retardation distance, when the two beams are recombined. On the other hand, the optical path is measured mathematically by taking the physical path (L) and the optical path (2L), which is the actual distance of the reflected light. The light would travel a physical length of L and an optical path of 2L to return to the beamsplitter, if the moving mirror and the stationary mirror were to be located at the same distance from the beam-splitter. Thus, when the movable mirror travels small amounts of length x, the split beams of light travels a distance of 2(L + x) [37].

Constructive interference happens when the two electromagnetic waves are in phase, and a retardation is a whole number multiplied by the wavelength, $n\lambda$, and n=1,2, 3, so that $2x=n\lambda$ [37]. When the retardation of the electromagnetic wave is half of an integer, $\frac{1}{2}\, n\lambda$, n=1,3,5, it goes through a deconstructive interference; where $2x= \frac{1}{2}n\lambda$ [37]. The output beam has an intensity dependent on the amount of constructive interference. This relationship is significant because it enables a function of the optical path difference and wavelength of the incident radiation to be formulated. There could also be no retardation, which yields a maximum intensity and leads the beams of light to interfere constructively. An interferogram is then created as a function of optical path difference/retardation and recorded at the detector [36].

For a monochromatic source in an interferogram, only one wavelength would be described with a cosine function. The Fourier transform in the interferogram would produce a single peak in the spectrum, which is helpful for analysis and calibration. However, in experiments, the infrared source of the instrument is made up of many cosine functions, and the

interferogram consists of the sum of all continuous distribution of wavelengths in the beam. The signal forming the interferogram is integrated to obtain a Fourier transform spectral amplitude. This mathematical approach uses the cosine function to obtain the single beam spectrum. An example of an interferogram for a broad IR source is presented in Figure 2.8.

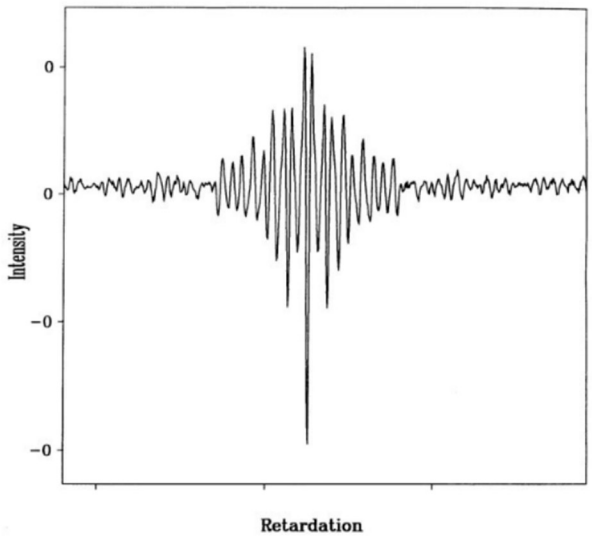

Figure 2.8: A plot showing the intensity detected at the detector as a function of retardation and known as a "broadband IR source interferogram." [37]

Also, since different path lengths and light beams that travel through various media are taken to develop alternating interference patterns at the detector, the shape of an interferogram usually reflects this phenomenon and becomes different. It will depend on the characteristics of the beamsplitter and light source used. Another example supporting this remark is presented in Figure 2.9 for the KBr beamsplitter and the globar IR lamp source [45]. In the right side of this image is shown an example of a recorded spectrum after applying the Fourier transform process. The characteristics sharp features observed in this spectrum are representative of the chemical structural arrangement of the atoms and their bonds' lengths existing in a measured sample. As previously mentioned, is unique for each sample.

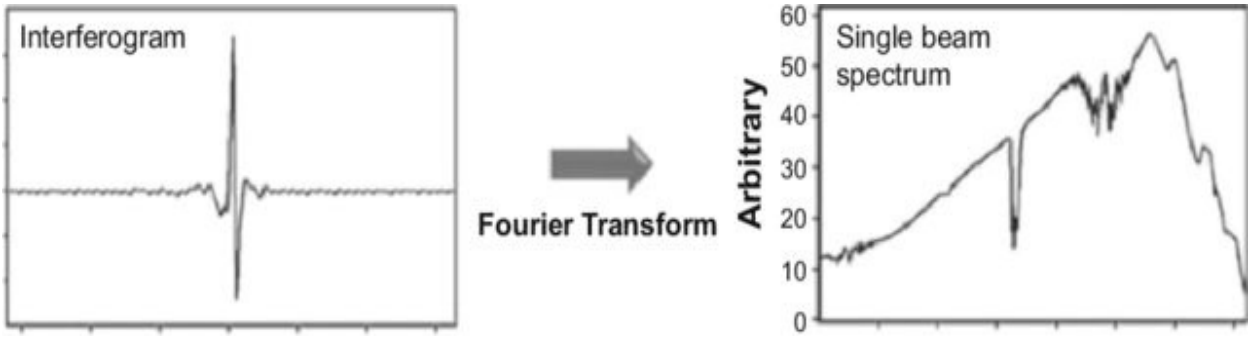

Figure 2.9: Fourier transformation interferogram to create a spectrum.[45]

Finally, an image of the Bruker FTIR-IFS 66v interferometer employed in the current data recording is shown in Figure 2.10. This system is also located in the Optical Spectroscopy and Microscopy laboratory at UTEP.

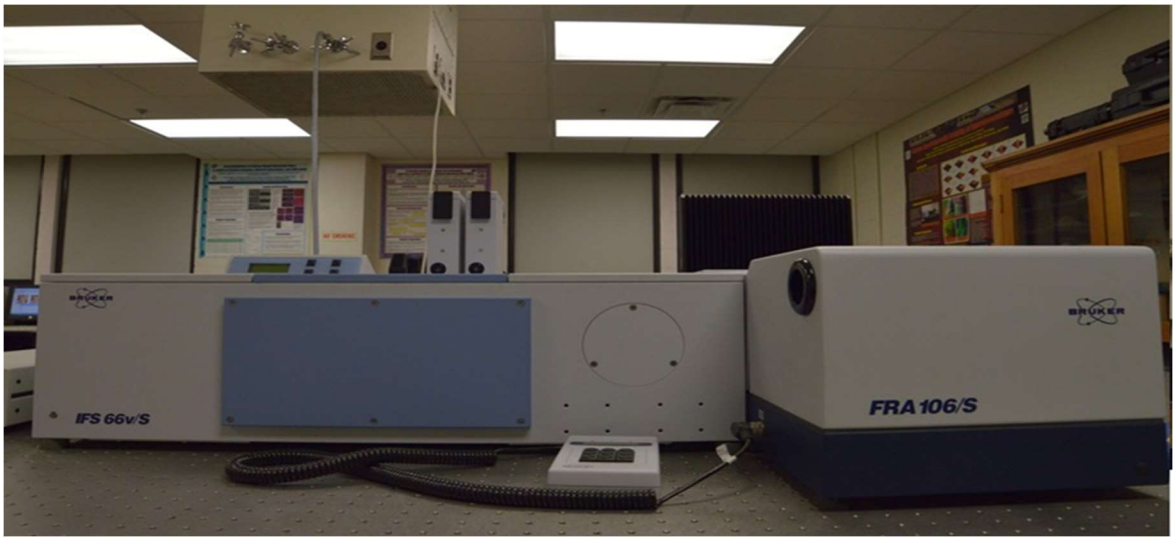

Figure 2.10: The Bruker IFS 66v Fourier Transform Infrared Interferometer (FTIR) system used in the study in the optical spectroscopy and microcopy lab at the University of Texas at El Paso.

2.7 Experimental Recording

The spectra of transmitted (T) or absorbed (A) infrared radiation by the sample as a function of frequency are usually recorded. Two steps should be taken to obtain good quality

transmission or absorption spectra. The first one consists on recording the intensity $I_0(v)$, which is a reference/background that is taken without any sample. Since it is also the background noise of the detector, this recording indirectly assure the functionality of the system. To analyze a sample, next, the intensity transmitted $I_T(v)$ through the sample will be recorded. The computer automatically calculates the transmittance, which is the infrared spectrum obtained, $T = I_T(v)/I_I(v)$ [37]. A ratio of the transmitted beam over the reflection-corrected incident beam can be obtained in three different regions of the infrared spectrum, namely the near infrared (NIR) in the 12500 cm^{-1} to 4000 cm^{-1} regions, mid infrared (MIR) in the 4000 cm^{-1} to 400 cm^{-1} regions, and the far infrared (FIR) in the 400 cm^{-1} to 5 cm^{-1}.

A factor affecting the spectra is how controlled the system is, meaning for how long the chamber is kept at the atmospheric pressure. The system shown in Figure 2.10 is a vacuum based system that allows high resolution data recording. Especially in the FIR region, where water absorption and impurities could negatively affect the background reference I_0, it is important to minimize such unwanted influence to improve data quality.

2.8 Density Functional Theory

The electronic structure of atoms, molecules, and solids can be calculated using density functional theory (DFT), a quantum-mechanical (QM) approach used in chemistry and physics. The Schrodinger equation for a many-body system may be reduced to a single-particle independent Schrodinger equation, solved numerically using density functional theory [46]. However, the theory is based on electron density rather than the wave function of the molecule. The number of degrees of freedom in the system must be reduced as much as feasible. The computation is accelerated when the electron density is used. The electron density is a function

of three variables: x, y, and z. The many-body electronic wave function is a function of 3N variables (the coordinates of all N atoms in the system). The precise interpretation of conformationally related intensity fluctuations becomes essential for spectroscopic studies of more extensive, physiologically important systems. Obtaining the theoretical spectra from DFT not only predicts the experimental spectra but can also help confirm the presence of a molecule.

CHAPTER 3

OPTICAL IDENTIFICATION OF NDGA'S MORPHOLOGICAL FORMS

3.1 Introductory Remarks

A combined theoretical and experimental analysis is used to examine spectroscopically the NDGA biomechanistic structure-function. The results are expected to provide additional information for determining the relationships between potential NDGA structural forms with their therapeutic or toxic effects in preventing and treating various diseases. As mentioned earlier, the medicinal and antiviral properties of *Larrea Tridentata* have been studied *in vivo* and *in vitro*. However, the accurate distinction between morphological changes of NDGA has yet to be identified optically, which is the intent of this study.

3.2 Materials and Methods

NDGA (C18H22O4, >97 %) was acquired from Sigma-Aldrich (Sigma-Aldrich Co.) and utilized as received. The Raman measurements were conducted under ambient circumstances using an alpha 300RAS WITec system (WITec GmbH, Ulm, Germany) and an air objective lens of 20X (Olympus, Japan) with an aperture (NA) of 0.4, using an excitation of frequency-doubled neodymium–aluminum–garnet (Nd: YAG) laser at 532nm. The laser was maintained at a constant power output of a few mW. Accumulations of 20 Raman spectra were collected, each in 500 milliseconds and resulting in total acquisition times of 10 seconds and 4 cm^{-1} of spectral resolution [47].

The IR spectrum analysis in this work was conducted using a commercial rapid scan vacuum-based Bruker FTIR-IFS 66v (Bruker Optics Inc., Billerica, MA) system. A deuterated

lanthanum alanine doped triglycine sulfate (DLaTGS) detector and potassium bromide (KBr) beam-splitter were used to make measurements in the mid-IR region (Bruker Optics Inc.). NDGA samples were embedded in a polycrystalline KBr matrix, and the samples for IR measurements were prepared as pellets. The spectra were produced by accumulating 256 scans at a resolution of 4 cm^{-1}. The data were recorded in vacuum and Fourier-transformed into a throughput spectrum [47].

Computational analysis was performed using *Gaussian-16* analytical suite software for the quantum chemical density functional calculations. Before determining vibrational frequencies, an energy optimization was conducted. The Becke three hybrid exchange [48] and the LeeYang-Parr correlation functional, B3LYP [49], were employed for these analyses. The molecular form was also calculated using a 6-311++G (d, p) basis set. The Gaussian-16 output data were parsed using an in-house C++ technique and then translated to MATLAB version r2016a. In the Raman computed data, a previously documented approach was used to convert Raman activities into relative Raman intensities [50]. In the current conversion for the laser excitation, a value of 532 nm = 18,796.99 cm^{-1} was chosen. To facilitate data visualization, all predicted peak intensities were standardized by appropriate factors to match those obtained in the experiment. For easier viewing, Lorentzian band with a full width at half maximum (FWHM) of 7 cm^{-1} were also used to expand the theoretically determined lines [47].

3.3 Optical Identification of NDGA Morphological Conformations

As mentioned previously, NDGA contains four phenolic hydroxyl groups that function as proton donors or acceptors (see Figure 1.3). However, the molecule only dissociates/oxidizes in extremely basic conditions with an approximate pK_a value of 9.3 [18]. For investigations in

aqueous solutions, the compound's insolubility in water requires its previous solvation in small quantities of dimethyl sulfoxide (DMSO), acetonitrile, or methanol [18]. Due to these conditions, NDGA's neutral unoxidized molecule form is most expected in a powder form, which is first analyzed here [47].

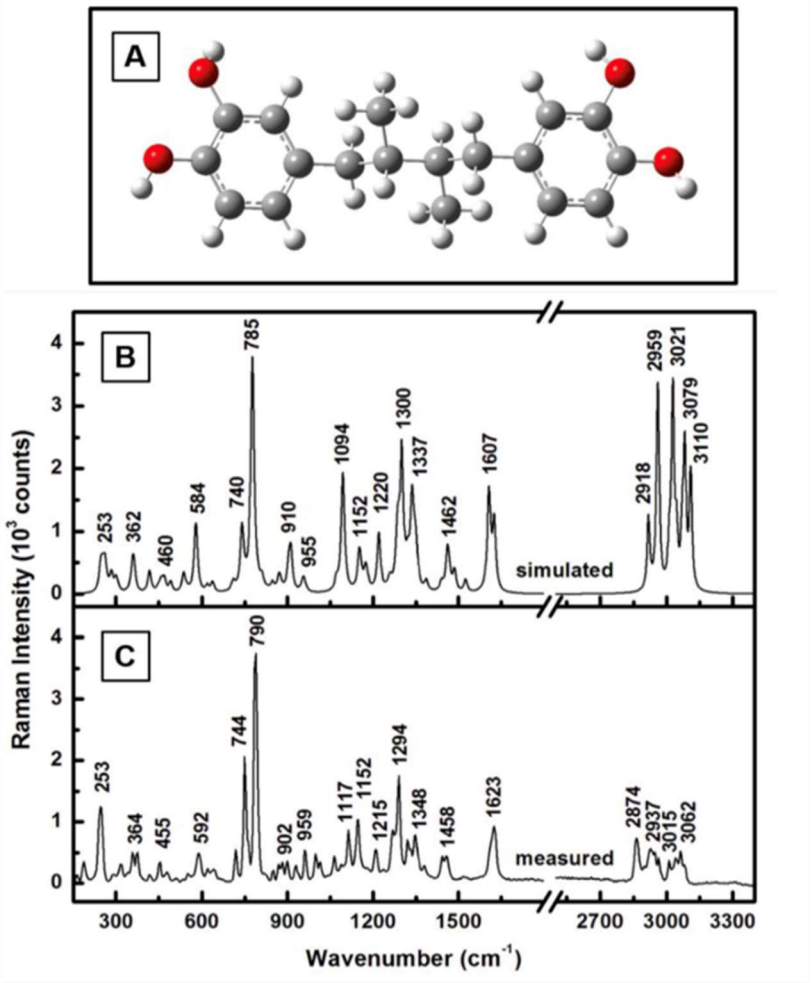

Figure 3.1 (**A)** Neutral structural depiction of nordihydroguaiaretic acid (NDGA). Red is used for oxygen atoms, dark gray for carbon atoms, and light gray for hydrogen atoms. **(B)** Furthermore, **(C)** is theoretically estimated and experimentally observed Raman vibrations of NDGA, respectively. The Raman spectra of the standard NDGA powder were recorded [47].

Figure 3.1A depicts the NDGA's energetically optimized molecular structure with its unoxidized hydroxyl groups. The corresponding theoretical/simulated Raman vibrations obtained by DFT computation and the experimentally measured are presented in Figure 3.1B and Figure 3.1 C, respectively. This compact representation of the results allows for easier visual comparison between theoretical and measured results [47]. To include all regions of interest in the same spectral image, a break between 1800 and 2500 cm^{-1} was performed in the spectra shown in Figures 3.1B and 3.1C. Also, a scaling factor of 0.98 was applied to the theoretically obtained spectrum, to enable better agreement with the one experimentally acquired. Figure 3.1B shows the most dominant Raman frequency at 785 cm^{-1}, which may be interpreted as a Raman spectroscopic fingerprint for neutral NDGA and agrees with the measured Raman frequency of 790 cm^{-1} in Figure 3.1C.

The measured 790 cm^{-1} most noticeable frequency corresponds to the molecule's in-plane ρ(C=C) rocking, ν(C-O) stretching, out-of-plane ω(CH_3) wagging, and benzene ring deformation. Other significant measured vibrational modes were recorded at 744 cm^{-1} (calculated at 740 cm^{-1}), 1294 cm^{-1} (calculated at 1300 cm^{-1}), and 1623 cm^{-1} (calculated at 1607 cm^{-1}). All of these vibrations are primarily caused by stretching and rocking of the molecule's two catechol ring moieties, which occur in-plane. In addition, weak out-of-plane ω(CH_2) and ω(CH_3) wagging, and τ(CH_3) twisting contribute in a less substantial way. The ν_s(CH_3) and ν_s(CH_2) symmetric stretching of the aliphatic chain predominate in the higher frequency range between 2800 cm^{-1} and 3100 cm^{-1}. A comparison of the Raman spectra in Figures 3.1B and 3.1C shows that the theoretically computed and measured peak frequencies are in good agreement, with average differences of 5 ± 2 cm^{-1}. Table 3.1 summarizes the observed and computed values of the Raman vibrational modes and their tentative assignments [47].

Table 1. Tentative assignments of the theoretically calculated and experimentally recorded Raman vibrations of NDGA.[47]

Calculated (cm^{-1})	Measured (cm^{-1})	Assignment
253(m)	253(s)	in-plane ρ(CH_3) strong rocking; out-of-plane ω(O-H) weak wagging
362(m)	364(m)	in-plane ρ(C-H) strong aromatic rocking; out-of-plane ω(C-O-H) weak wagging; out-of-plane weak benzene ring bending
460(w)	455(w)	in-plane ρ(C-O-H) rocking; ρ(CH_2) rocking; ν(C-O) stretching; out-of-plane ω(C-H) weak wagging; benzene ring deformation
584(m)	592(m)	in-plane strong ρ(C-O-H) rocking; ρ(CH_2) rocking; in-plane benzene ring rocking
740(m)	744(s)	in-plane ν(C=C) stretching; ν(C-O) stretching; out-of-plane ω(CH_2) and ω(CH_3) weak wagging; benzene ring bending
785(vs)	790(vs)	in-plane ρ(C=C) rocking; ν(C-O) stretching; out-of-plane ω(CH_3) very weak wagging; benzene ring deformation
910(m)	902(w)	in-plane ν(CH_2) stretching; ν(CH_3) stretching; ρ(C-H) rocking; ν(C-O-H) stretching; benzene ring deformation
955(w)	959(m)	in-plane ν(C=C) stretching; ν(CH_2) stretching; ρ(CH_2) rocking; benzene ring bending
1094(s)	1117(m)	in-plane ν(C-O-H) stretching; ρ(C=C) rocking; ρ(CH_3) rocking; ρ(CH_2) rocking; out-of-plane τ(CH_3) twisting
1152(m)	1152(m)	in-plane ρ(O-H) rocking; δ(C=C-C) bending; ρ(C-H) rocking; out-of-plane τ(CH_3) twisting
1220(m)	1215(m)	in-plane ρ(O-H) rocking; δ(C=C-C) bending; ρ(C-H) rocking; out-of-plane τ(CH_3) twisting; benzene ring deformation
1300(s)	1294(s)	in-plane strong benzene ring breathing; ρ(C-H) rocking; ν(C-O) stretching
1337(m)	1348(m)	in-plane ν(C=C) stretching; ν(C-O-H) stretching; ρ(C-H) aromatic rocking; out-of-plane ω(CH_3) weak wagging; out-of-plane τ(CH_3) weak twisting
1462(m)	1458(m)	in-plane ν(C-O) stretching; ρ(C-H) rocking; ; ρ(C=C) rocking; benzene ring deformation
1607(s)	1623(s)	in-plane ρ(C-O-H) rocking; ν(C=C) stretching; out-of-plane τ(CH_3) twisting
2918(m)	2874(s)	ν_s(CH_3) stretching; ν_s(CH_2) stretching; ν_s(CH) stretching
2959(vs)	2937(m)	ν_s(CH_3) stretching; ν_s(CH_2) stretching; ν_{as}(CH) stretching
3021(vs)	3015(m)	ν_{as}(CH_3) stretching; ν_{as}(CH) stretching
3079(s)	3052(m)	ν_{as}(CH_3) stretching; ν_{as}(CH_2) stretching
3110(s)		ν_{as}(CH_3) stretching; ν_{as}(CH_2) stretching

ν_{as}: asymmetric stretching; ν_s: symmetric stretching; δ: in-plane bending; ρ: in-plane rocking; ω: out-of-plane wagging; τ: out-of-plane twisting.

For a thorough analysis of the neutral NDGA form, complementary IR vibrations were studied and presented in Figure 3.2A-C [47]. Figure 3.2A shows the displacement vectors corresponding to the theoretically most noticeable IR vibrational mode at 1168 cm^{-1} (experimentally measured at 1190 cm^{-1}). This IR vibrations is associated with the compound four hydroxyl groups and can be consider as the IR fingerprint of neutral NDGA.

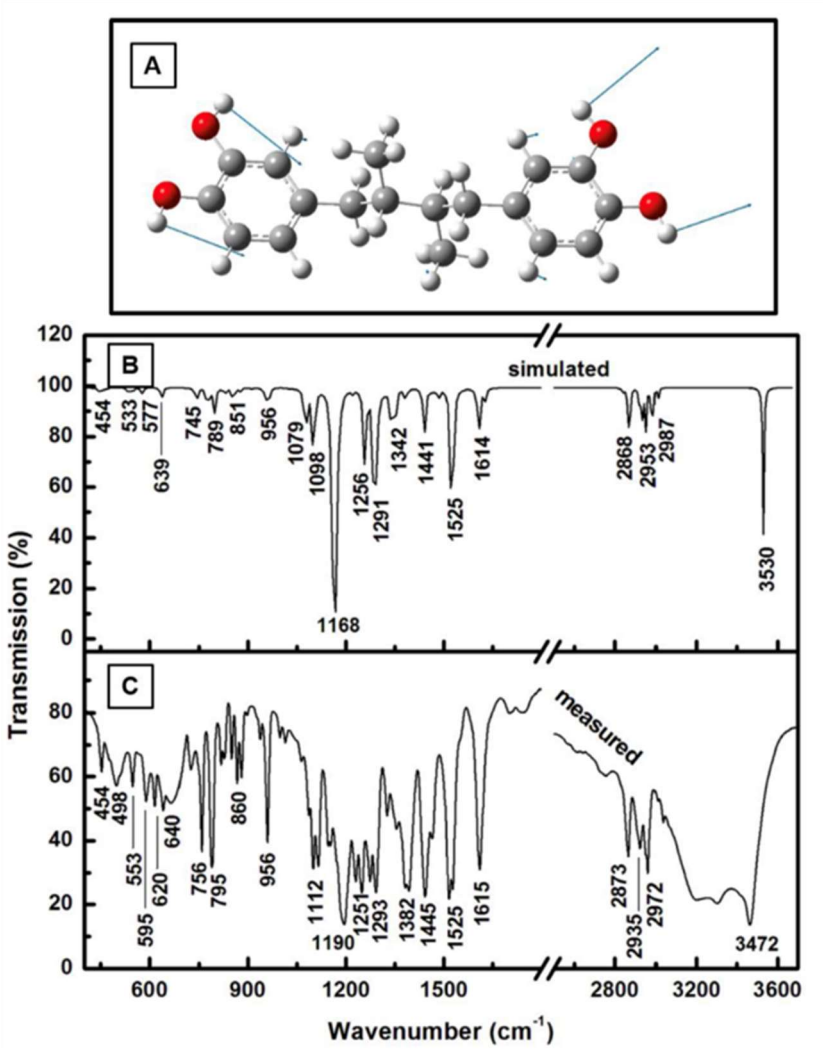

Figure 3.2 (A) Neutral nordihydroguaiaretic acid (NDGA) structural representation with displacement vectors for the strongest IR vibration at 1168 cm^{-1} shown by blue arrows. **(B) and (C)** Neutral NDGA's infrared transmission spectra, as calculated theoretically and as measured experimentally. For measurements, the KBr pellet method was employed.[47]

The 1190 cm^{-1} frequency corresponds to catechol's strong ρ(O-H) rocking and in-plane benzene stretching. Other intense IR absorptions are observed at 1112 cm^{-1} (calcd. at 1098 cm^{-1}), 1251 cm^{-1} (calcd. at 1256 cm^{-1}), 1293 cm^{-1} (calcd. at 1291 cm^{-1}), 1445 cm^{-1} (calcd. at 1441 cm^{-1}), 1525 cm^{-1} (calcd. at 1525 cm^{-1}), and 1615 cm^{-1} (calcd. at 1614 cm^{-1}) [47]. Once more, the catechol rings' deformations and in-plane breathing are principally responsible for these vibrations, with additional contributions coming from the aliphatic chain's fragments such ρ(CH_3) rocking and τ(CH_3) twisting, as well as the aromatic out-of-plane τ(C-H) twisting.

Another remark worth pointing out is the experimentally measured IR vibrations in Figure 3.2C having significantly stronger intensities than the ones calculated in Figure 3.2B. This is attributed to the sensitivity of IR measurements to water absorptions that are not considered in the simulated IR. The significant IR absorption in Figure 3.2C in the 3000–3500 cm^{-1} area, which is the typical zone for water absorption, further supports the statement of sensitivity to water. However, as in the case of the Raman data, a good agreement between the IR predicted and experimentally measured data is seen in Figures 3.2B and 3.2C, with an average difference in vibrational frequencies of 7 ± 4 cm^{-1} in the 400 – 1800 cm^{-1} range and 11 ± 4 cm^{-1} in the 2500 – 3700 cm^{-1} region. In this situation, the estimated frequencies for lower wavenumbers (400 – 1800 cm^{-1}) and higher wavenumbers (2500 – 3700 cm^{-1}) are scaled in the theoretically obtained spectrum by 0.98 and 0.96 [47].

Table 2 provides the measured and theoretically computed values of the IR vibrational modes and their tentative assignments [47].

Table 2. Tentative assignments of the theoretically calculated and experimentally recorded IR vibrations of NDGA. [47]

Calculated (cm^{-1})	Measured (cm^{-1})	Assignment
454(vw)	454(w)	out-of-plane ω(C-H) wagging; ν_{as}(C=C-C) stretching; ρ(CH_2) rocking; benzene ring bending
	498(w)	out-of-plane ω(CH_3) wagging; in-plane ρ(C-O-H) rocking; ρ(CH_2) rocking; benzene ring deformation
533(vw)	553(w)	ρ(C=C) rocking; δ(CH_2) and δ(CH_3) bending; out-of-plane τ(CH) and benzene ring twisting
577(vw)	595(w)	in-plane ρ(C-O-H) and benzene ring rocking; out-of-plane aromatic chain ω(CH_2) and ω(CH_3) wagging
	620(w)	out-of-plane τ(CH) twisting; ω(C=C-C) wagging; out-of-plane aromatic chain ω(CH_2) and ω(CH_3) wagging
639(vw)	640(m)	out-of-plane τ(CH) twisting; ω(C=C-C) wagging; out-of-plane aromatic chain ω(CH_2) and ω(CH_3) wagging
745(vw)	756(s)	in-plane δs(C=C-C) scissoring; ν(CH_2) stretching; in-plane ν_s(OH) symmetrical stretching
789(w)	795(s)	in-plane ν_s(C-O) symmetrical stretching; in-plane δs(C=C-C) scissoring; out-of-plane ω(C-H) and ω(CH_3) wagging
851(vw)	860(m)	out-of-plane ω(C-H) wagging; ρ(CH_2) rocking; aromatic chain ν_s(CH_2) and ν_s(CH_3) stretching
956(w)	956(s)	in-plane ν_s(C=C-C) and ν(C-OH) stretching; aromatic ν(CH_2) stretching; ρ(C-H) rocking; out-of-plane τ(C-H) twisting; out-of-plane ω(CH_3) wagging
1079(m)	1098(s)	in-plane ν(C=C) stretching; ρ(O-H) rocking; ρ(CH_3) rocking; τ(C-H) twisting
1098(s)	1112(s)	in-plane δs(C=C) scissoring; ρ(C-O-H) rocking; ρ(CH_2) rocking; ρ(CH_3) rocking; in-plane ν_s(CH_2) symmetrical stretching
1168(vs)	1190(vs)	in-plane strong ρ(O-H) rocking; in-plane ν_{as}(C-H) and benzene ring asymmetrical stretching; ρ(CH_3) rocking
1256(s)	1251(s)	out-of-plane τ(C-H) twisting; out-of-plane ρ(CH_3) rocking; ν(C-OH) stretching
1291(s)	1293(s)	strong benzene ring breathing; ρ(C-H) rocking; ρ(CH_2) rocking;
1342(m)	1382(s)	ρ(O-H) rocking; ρ(C-H) rocking; ρ(CH_3) rocking
1441(m)	1445(s)	in-plane ν_{as}(C-C-O) strong stretching; ρ(O-H) rocking; ρ(C-H) rocking; out-of-plane τ(CH_2) twisting
1525 (s)	1525(s)	ρ(C-H) rocking; δ_S(C-O-H) scissoring; in-plane benzene ring symmetrical stretching
1614(m)	1615(s)	in-plane strong benzene ring asymmetrical stretching; ρ(O-H) rocking; δ_S(C-O-H) scissoring; out-of-plane τ(CH_2) twisting
2868(m)	2873(m)	in-plane strong ν_s(CH_3) and ν_s(CH_2) stretching; ρ(C-H) rocking;
2953(m)	2935(m)	in-plane ν_{as}(CH_3) and ν_{as}(CH_2) stretching
2987(m)	2972(m)	in-plane ν(C-H) stretching; ρ(C-H) rocking
3530(s)	3472(s)	in-plane ν(O-H) strong stretching

ν_{as}: asymmetric stretching; ν_s: symmetric stretching; δ: in-plane bending; ρ: in-plane rocking; ω: out-of-plane wagging; τ: out-of-plane twisting.

NDGA has also been known to be unstable in aqueous conditions, with an autoxidation process happening more frequently at an increasing pH [51][52]. NDGA has a different electro-oxidation process than other catechols that follow a two-electron redox reaction [51]. It has been proposed that intermediate semi-quinone radicals are formed first, mostly of cations, due to compound rapid deprotonation, transitioning to either para-quinone methide (one-step electron transfer) or ortho-quinone (one-step two-electron transfer) forms [53][54]. This process also includes the possibility of additional oxidation of the ortho-quinone form by a second one-step two-electron transfer, resulting in a fully oxidized NDGA. Figure 3.3 depicts a simplified diagram of the NDGA oxidation process, with all forms identified accordingly.

In Figures 3.4A–D, Figure 3.6A–D, and Figure 3.8A–D are shown the structural representations of NDGA para-quinone methide form, ortho-quinone form, and the completely oxidized configuration, with their Raman and FTIR theoretical calculations of vibrational signatures [47] As before, a for more straightforward visualization and identification of spectroscopic differences between these NDGA forms, the most intense vibrational modes observed for both Raman and IR displacement vectors are represented by blue arrows in Figures 3.4A and 3.4B, Figures 3.6A and 3.6B, and Figures 3.8A and 3.8B. Similar to previous cases, for consistency between experimental and theoretical results, a 0.98 scaling factor was applied to the 150-2000 cm^{-1} spectroscopic region that is considered essential in optical identification of NDGA's forms. Also, the region at higher frequencies, which is heavily dominated by the water absorption, is not represented in these figures. In what follows we are going to discuss first the para-quinone methide form of the compound that is presented in Figure 3.4A–D.

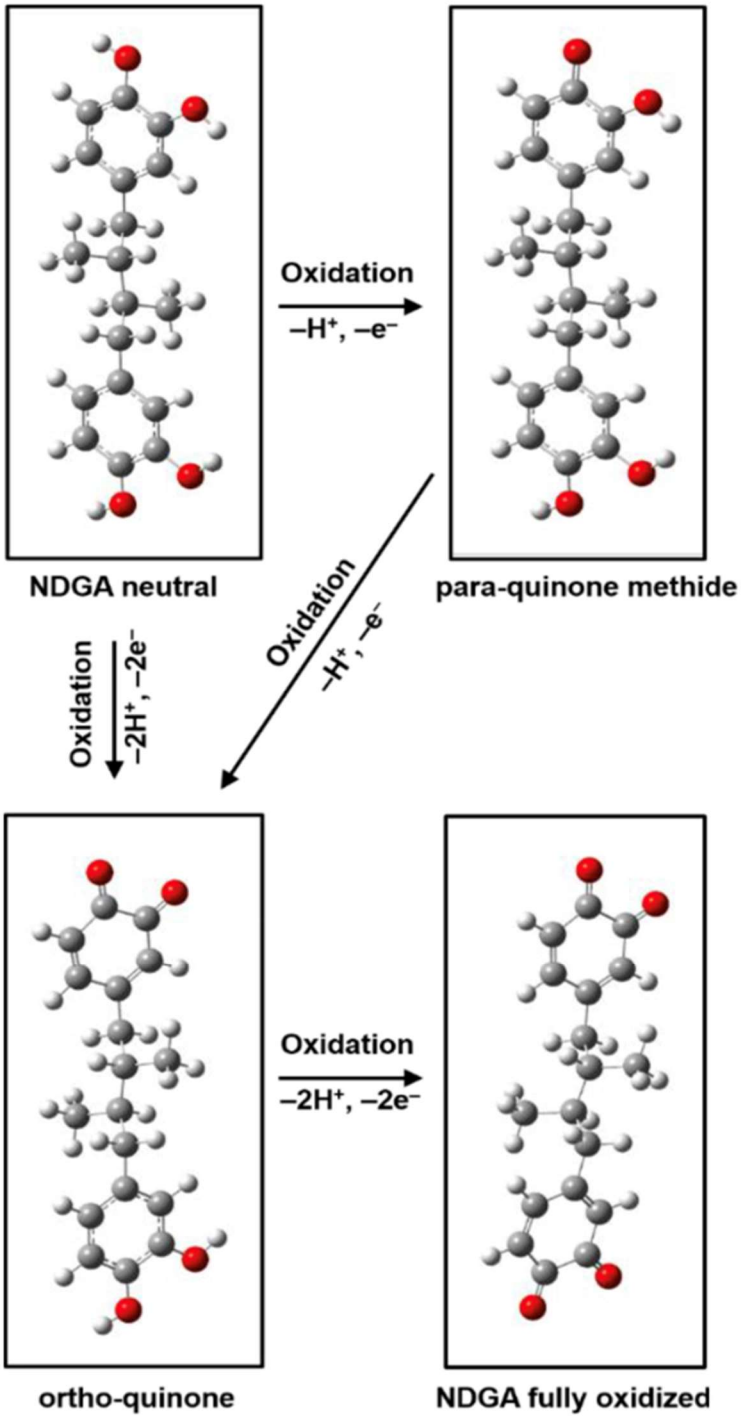

Figure 3.3 Diagram of the NDGA oxidation process, which includes para-quinone methide, ortho-quinone, and the fully oxidized form, as labeled [47].

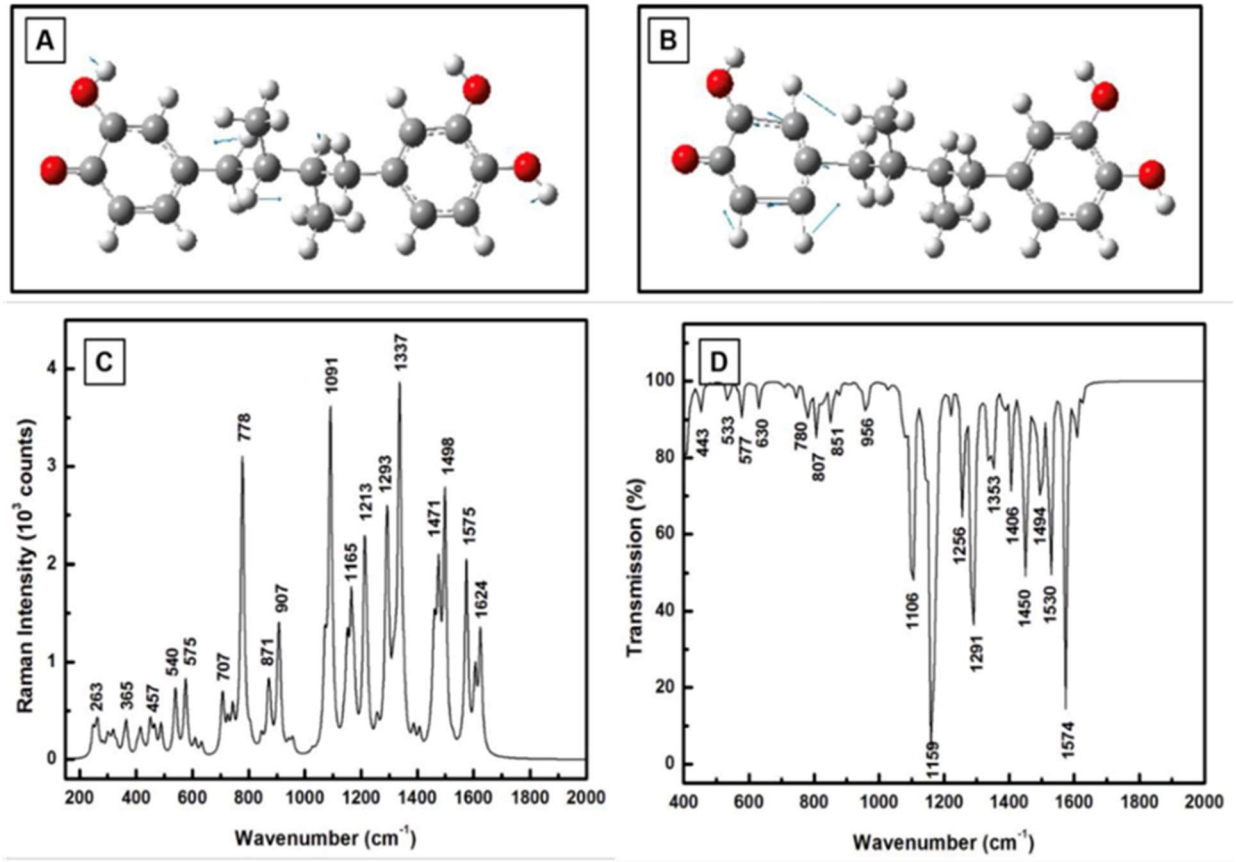

Figure 3.4 (A) and **(B)** The displacement vectors for the most intense Raman vibration at 1337 cm^{-1} and IR vibration at 1159 cm^{-1} are represented by blue arrows in the para-quinone methide structural model of NDGA. **(C)** and **(D)** Para-quinone methide's Raman theoretical calculations and infrared vibrational spectrum.[47]

The displacement vectors for the Raman vibration at 1337 cm^{-1} and the IR vibration at 1574 cm^{-1} are represented by blue arrows in Figures 3.4A and 3.4B. They can be considered as fingerprint signatures for the para-quinone methide form. The Raman vibrational mode at 1337 cm^{-1} is linked to the catechol deformation caused by in-plane ν(C=C) stretching, ρ(O-H), and ρ(C-H) rocking, as well as aliphatic chain deformation caused by ρ(CH_2) rocking and out-of-plane ω(C-H) weak wagging. Strong ν(C=C) stretching, strong ρ(C-H) rocking, and weak

ν(C=O) stretching and ρ(O-H) rocking are associated with the 1574 cm^{-1} IR vibrational mode [47].

While in Figure 3.4 A and Figure 3.4 B are imaged the most dominant Raman and IR vector motion/vibrations for this form with only one oxidized hydroxyl group (i.e., the para-quinone methide form), in Figure 3.4 C and Figure 3.4 D are shown the overall calculated spectra. In figure 3.4C, in addition to the Raman signature at 778 cm^{-1}, which was theoretically calculated at 785 cm^{-1} for the neutral NDGA form (see Figure 3.1B), the spectrum of para-quinone methide form contains additional powerful Raman lines at 907, 1091, 1165, 1213, 1293, 1337, 1471, 1498, 1575, and 1624 cm^{-1} [47]. The IR spectrum of this form, shown in Figure 3.4D, demonstrate a similar spectroscopic activity, with a noticeable rise in the intensities of absorption lines at 1106, 1159, 1291, 1450, 1530, and 1574 cm^{-1} [47].An easier visual comparison between the Raman and IR spectra of neutral and para-quinone forms of NDGA can be depicted in Figure 3.5 A-D.

In the case of NDGA neutral form, the Raman 785 cm^{-1} and IR 1168 cm^{-1} strong vibrations/signatures are observed in Figure 3.5A and Figure 3.5B, respectively. Although these vibrations appear in the corresponding Raman and IR spectra of para-quinone methide form (see Figure 3.5C and Figure 3.5D), they are slightly shifted by 7 cm^{-1} in the case of Raman and 9 cm^{-1} in the IR case. However, in an experimental setting, these theoretically obtained shifts could be too subtle to detect. Thus, other strong vibrations in the $900\ cm^{-1} - 1650\ cm^{-1}$ region of the Raman and IR spectra of para-quinone methide can be used to distinguish between these forms, such as the Raman vibration at 1337 cm^{-1} and the IR vibration at 1574 cm^{-1}.

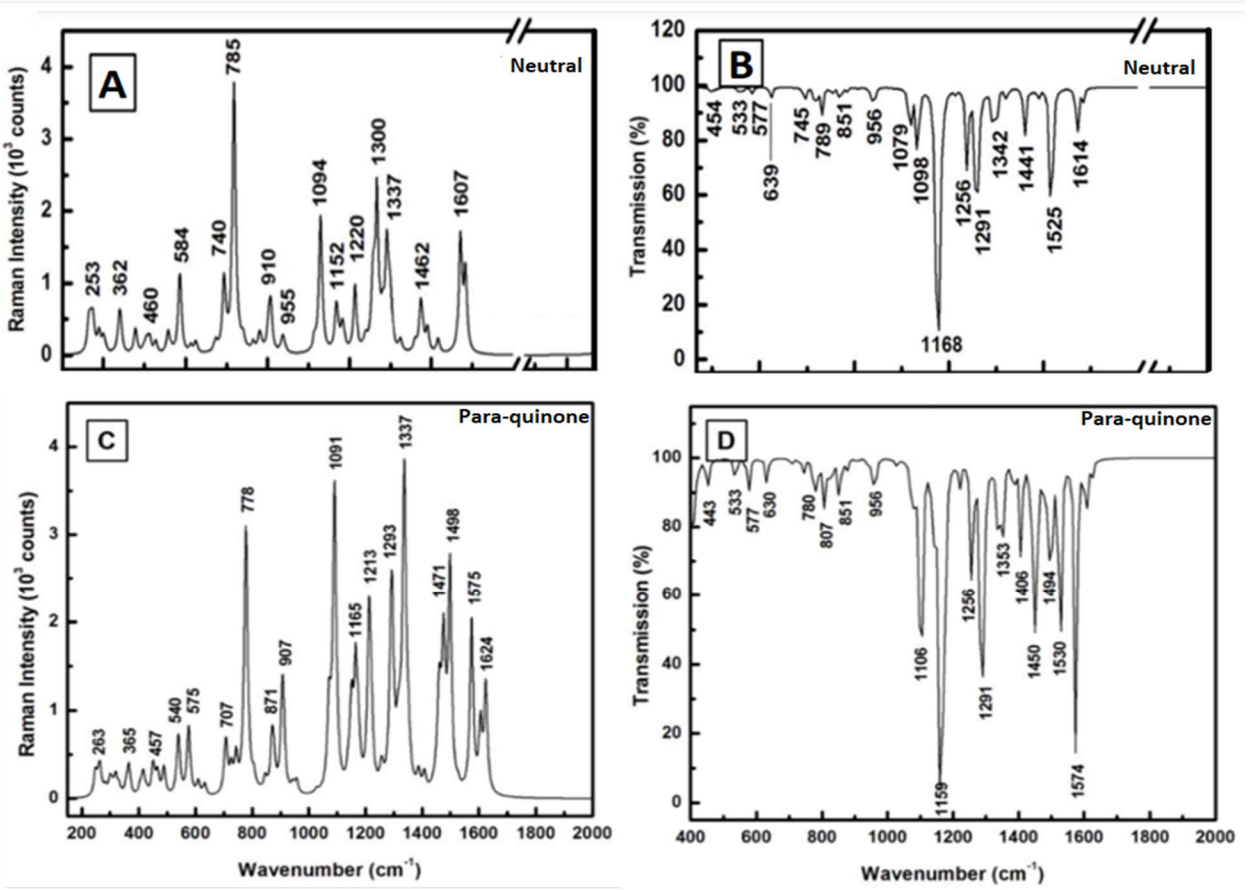

Figure 3.5 (A) and **(B)** represent theoretical observed Raman and IR vibrations of neutral NDGA, respectively. **(C)** and **(D)** represents theoretically observed Raman and IR vibrations for the para-quinone form of NDGA, respectively.

The next possible oxidation stage of NDGA when two of the compound's hydroxyl groups have been oxidized, the ortho-quinone form, is presented in Figures 3.6A-D. It has been proposed that the ortho-quinone form predominates at physiological pH values close to 7.4 [55][52]. The characteristic Raman and IR spectra of the ortho-quinone form are shown in Figures 3.6C and 3.6D, respectively, revealing a further change in the molecular vibrations of NDGA [47]. The dramatic intensity increases of the 1583 cm^{-1} and 1697 cm^{-1} Raman vibrations and the 1663 cm^{-1} and 1144 cm^{-1} IR vibrations are the most noticeable differences;

they can be considered as optical signatures for the ortho-quinone form. The blue arrows in Figures 3.6A and 3.6B depict the displacement vectors of the 1583 cm^{-1} Raman peak and the 1663 cm^{-1} absorption line, respectively. . These vibrational lines in the 1700 cm^{-1} frequency region correspond to the benzene ring's strong in-plane (C=O) and (C=C) stretching, (O-H) rocking, and out-of-plane (CH_2) wagging. They provide another evidence for the NDGA's morphological change caused by the oxidation process [47].

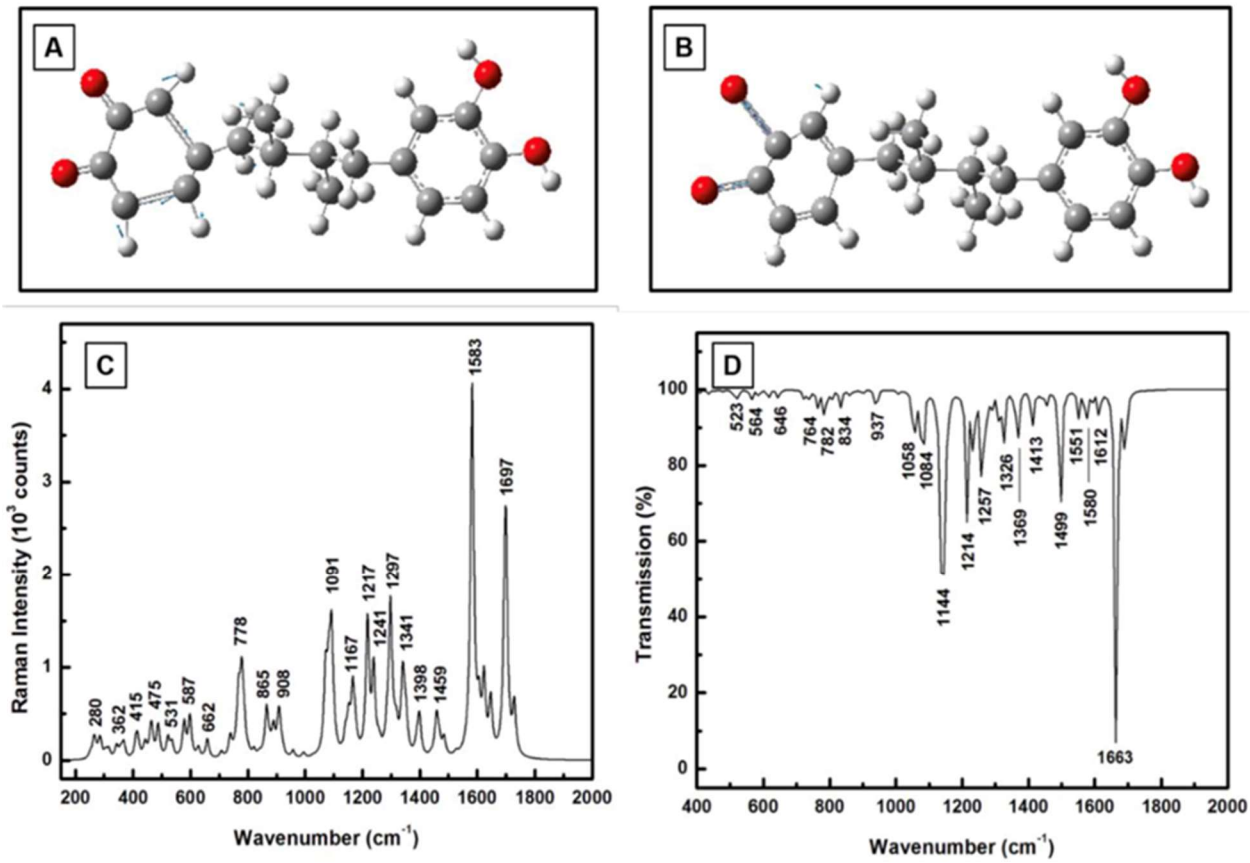

Figure 3.6 (A) and **(B)** Ortho-quinone structural model of NDGA with blue displacement vectors for the strongest Raman vibration at 1583 cm^{-1} and the strongest IR vibration at 1663cm^{-1} , respectively. **(C)** and **(D)** Ortho-quinone NDGA form's Raman theoretical calculations and IR vibrational spectra.[47]

An easier visualization of vibrational changes occurring in NDGA transformation from para- to ortho-quinone form can be seen in Figure 3.7, where the Raman and IR calculated

frequencies for these forms are presented. The 778 cm^{-1} Raman vibration of the para-quinone methide form (see Figure 7A) is still visible in the Raman spectrum of ortho-quinone form (see Figure 3.7C). However, its strength is significantly lower in the latter case. Much lower intensities for all Raman peaks in the 1000 – 1500 cm^{-1} frequency range are also seen in Figure 3.7, which are equivalent to those seen in the spectrum of the neutral form (Figure 3.1B). Figure 3.7D shows an IR decrease in the intensity of the 1144 cm^{-1} absorption line feature (compared to 1159 cm^{-1} para-quinone line) and a considerable rise in the 1663 cm^{-1} feature (compared to the 1574 cm^{-1} para quinone line). These decrease and/or increase in some of the IR vibrational lines, as well as the Raman 778 cm^{-1} decrease, are direct evidence of a continuous transformation of NDGA with oxidation. It is also enabling a differentiation between the compound's forms.

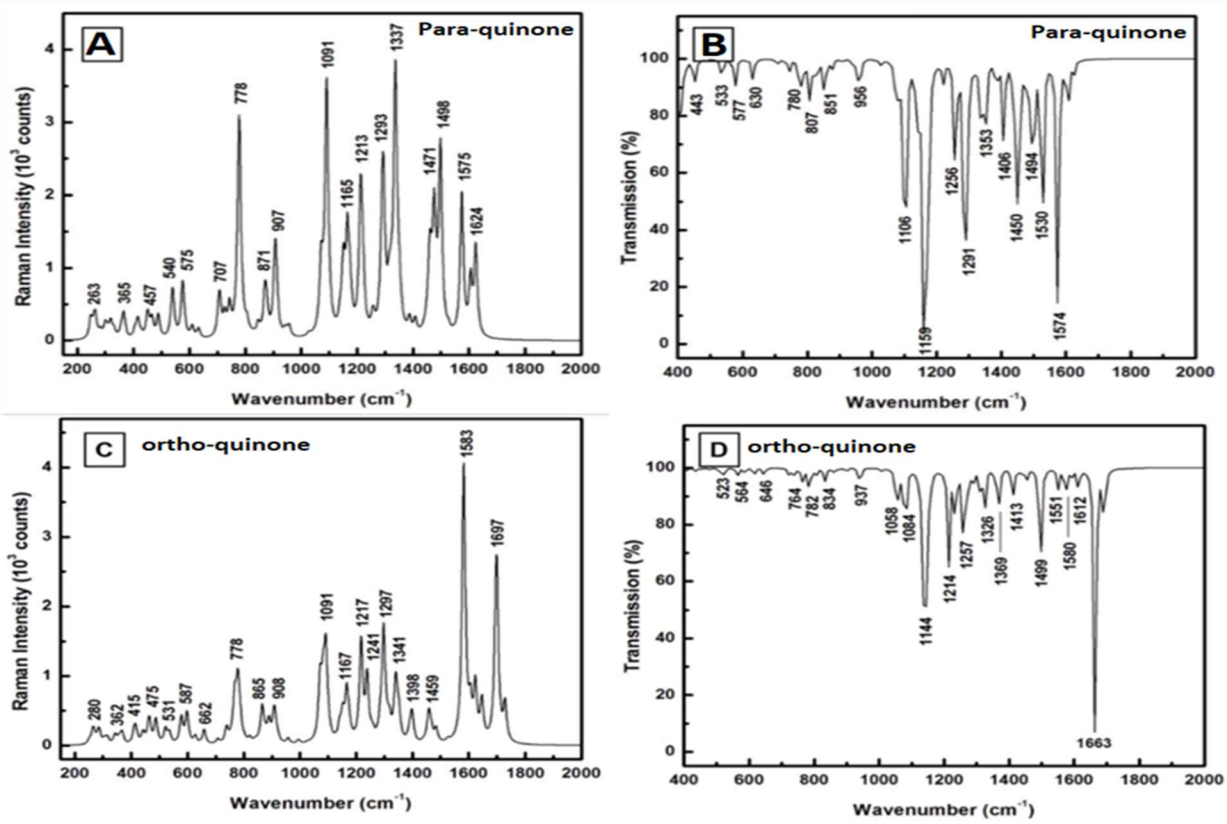

Figure 3.7 (A) and **(B)** present simulated para-quinone NDGA's Raman and IR spectra, respectively. **(C)** and **(D)** present simulated ortho-quinone NDGA's Raman and IR spectra, respectively.

Fully oxidized form of NDGA is presented in Figure 3.8. Although a fast visual comparison of the Raman and IR spectra of ortho-quinone with those of fully oxidized NDGA form that are shown in Figures 3.8C and 3.8D does not reveal any noticeable spectroscopic changes, a closer analysis reveals that certain discrepancies do exist. For example, the often-seen Raman vibrational line at 780 ± 5 cm^{-1} has a substantially lower strength and broadens, changes to a lower frequency of about 764 cm^{-1}, and practically vanishes in fully oxidized NDGA. This behavior demonstrates that the NDGA neutral form has entirely oxidized all hydroxyl groups.

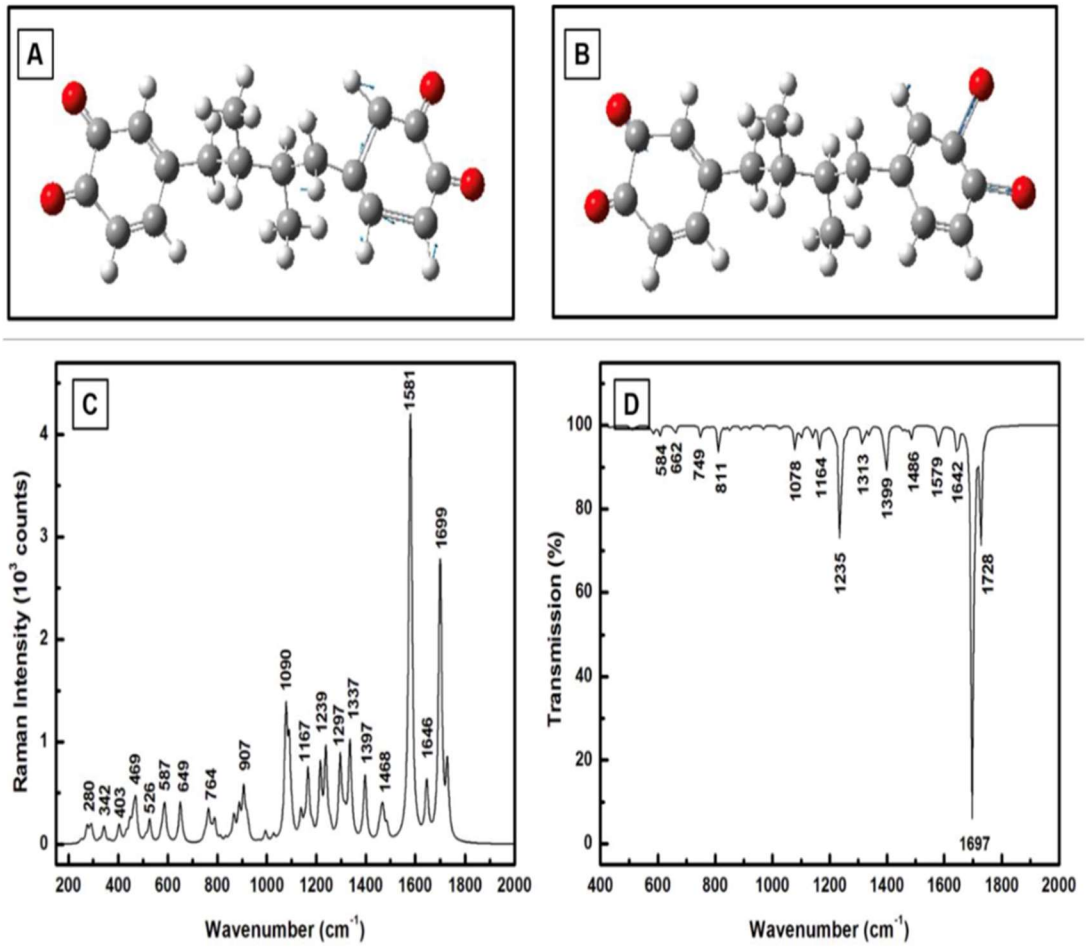

Figure 3.8 (A) and **(B)** NDGA's fully oxidized structural model with blue arrows representing displacement vectors for the strongest Raman vibration (1581cm^{-1}) and IR vibration (1697 cm^{-1}), respectively. **(C)** and **(D)** Fully oxidized NDGA form's Raman theoretically predicted and IR vibrational spectra.[47]

The emergence of the absorption line at 1235 cm^{-1} in the IR spectrum (Figure 3.8D) is also a significant spectroscopic modification. Because this vibration is associated with asymmetric (C-C) stretching and (O-H) rocking of the catechol, as well as out-of-plane (CH_2) wagging of the aliphatic chain, similar to the ortho-quinone's feature at 1144 cm^{-1} and the para-quinone methide's feature at 1159 cm^{-1}, it could be assumed that in the fully oxidized configuration this line shifts to a much higher frequency. The displacement vectors for the Raman signature at 1581 cm^{-1}, and the IR absorption at 1697 cm^{-1}, are represented with blue arrows in Figures 3.8A and 3.8B, respectively emphasizing the vibrational resemblance between the NDGA fully oxidized and ortho-quinone forms. These signatures are dominant vibrational lines observed for both NDGA oxidized configurations.

3.4 Concluding Remarks

We theoretically and experimentally evaluate NDGA's structural configurations from a spectroscopic approach using DFT calculations, Raman spectroscopy, and FTIR spectroscopy. The purpose was to optically provide new insights into which NDGA morphological conformation offers health advantages, and which one causes harm. The identification of vibrational signatures of NDGA's oxidized forms, which are assumed to be connected with the compound's toxicity were successfully obtained. The neutral form has primary vibrations at 785 cm^{-1} in the Raman spectrum (see Figure 3.1B) and at 1168 cm^{-1} in the IR spectrum (see Figure 3.2B) [47]. A downshift in these vibrations 778 cm^{-1} and 1159 cm^{-1} identifies the para-quinone methide form [47]. Another observation consists of a sharp decrease in the intensities of these lines in the case of the ortho-quinone form (see Figures 3.6C and 3.6D), with a nearly disappearance for a fully oxidized form (see Figures 3.8C and 3.8D) [47].

On the other hand, the Raman vibrations at 1582 cm^{-1} and 1698 cm^{-1}, as well as the IR vibration at 1680 cm^{-1}, become more prominent as the oxidation process continues [47]. Having in mind that a fully oxidized form is more likely to accumulate and create toxic effects in vivo the results obtained here are of significance for further employment of the compound as a potential drug. Due to similarity in vibrations of the fully oxidized form with the ortho-quinone one, the latter might have a contribution as well to the previously mentioned toxicological effects.

Only by accurately identifying and discriminating between the NDGA's morphological forms can its impact as a drug be achieved. Further explorations of the compound effects on gliomas are presented next; specifically, the NDGA influence on malignant glioblastoma.

CHAPTER 4

NORDIHYDROGUAIARETIC ACID THERAPEUTIC EFFECT ON BRAIN CANCER

4.1 Introductory Remarks

Glioblastoma multiforme (GBM) makes up 60% of all adult brain tumors and is the most prevalent and aggressive primary malignant tumor [56]. Even though the origins of this severe form of intracranial brain cancer are still mostly unknown, people diagnosed with it have a 10% chance of living an average of five years [16]. Brain cancer is highly infiltrative and persistent, which makes it hard to treat. Based on the identification of the morphological form of the molecule, an investigation of NDGA's therapeutic effects on GMB is desired and pursued in the current study.

Lung and breast cancer, which are causes of other malignant tumors contributors to metastasis in the human body, have been successfully treated *in vitro* with NDGA, [19][57][58][59]. Because of the therapeutic effects of NDGA on different types of cancer, we examine here its biological effects on the intracranial GMB brain tumor. The in vitro bio-structural changes of untreated and NDGA-treated GMB cells are analyzed using a combination of experimental Raman microscopy and computational methods. Statistical analysis has been used to distinguish between the concurrent changes that were detected experimentally for the Raman vibrational signatures of proteins, lipids, and nucleic acids. The information obtained, connected to NDGA's bioactivity, is extremely valuable for understanding the drug's therapeutic mechanisms. It is valuable to creating and testing innovative pharmacological treatments for brain cancer.

4.2 Sample Preparation

The samples used in this research were prepared at the Mayo Clinic in Rochester, Minnesota by collaborators using standard fixation procedure with a 4% paraformaldehyde solution on plain microscope glass slides. They were measured at The University of Texas at El Paso. The human glioblastoma GBM cell line was selected from the Mayo Clinic's National patient-derived xenografts repository. Previous publications described procedures for short-term explant culture [60]. They are as follow: for proliferative purposes, the cells were then plated in culture flasks (250 mL, Falcon, Corning, NY, USA). The cells were washed with phosphate buffer (PBS, 4-5 mL, pH 7.0; Roche Life Science, Mannheim, Germany) after the confluence of the cells reached 50%, and then they were separated from the flask by incubation in a trypsin-EDTA solution (37 ºC, 95% O_2/5% CO_2) for a couple of minutes. Fetal bovine serum (FBS, 10%, Thermo Fisher Scientific Inc., Waltham, MA, USA) was added following cell detachment to neutralize the trypsin.

The flask was filled with a standard culture medium that contained high glucose Dulbecco's Modified Eagle's Medium (DMEM; 500 mL; Gibco, Waltham, MA, USA), FBS (10%; 50 mL; Gibco, Waltham, MA, USA), and penicillin-streptomycin (1%; 5 mL; Gibco, Waltham, MA, USA). Afterward, a 50 mL centrifuge test tube holding the mixture containing the isolated GBM cells was spun down at 1200 rpm for 10 minutes. The cells were resuspended in 1.0 mL of DMEM after removing the supernatant. Trypan blue staining was used to determine the cell viability and count (0.4 %). The cells were resuspended in additional DMEM (17 mL) to clarify the media, and 3 mL of the suspended cells were plated onto coverslips that had been autoclaved and coated with poly-L lysine (1:10, final concentration). The cells were then transferred back to the incubator (37 ºC, 5% CO_2) after cell attachment to the coverslips. The cell

supernatants were checked for mycoplasma contamination at regular intervals using a MycoAlertTM Mycoplasma Detection Kit (catalog #: LT07-118; Lonza, Rockland, MI, USA), and the findings were negative. When compared to historical controls, short tandem repeat analysis was utilized to confirm the authenticity of the cells in each experiment.

The cell treatment with NDGA used the following procedure: first, 90 L of dimethyl sulfoxide solution (DMSO; Life Technologies, Carlsbad, CA, USA) was mixed with 30 mg of NDGA (Sigma-Aldrich, St. Louis, MO, USA). The final volume was changed to 1 mL once the NDGA powder had completely dissolved. This solution was further diluted in cell medium to concentrations of 100 μM and 250 μM NDGA for Raman experiments, and it was then utilized immediately to prevent any oxidation. The high-dosed GBM6 cells were incubated for 4 hours with a 250 μM concentration of NDGA, whereas the low-dosed GBM6 cells were treated for 24 hours with a 100 μM concentration of NDGA. Following the incubation, the cells were five-times washed with PBS before being fixed for 15 minutes with a 4% paraformaldehyde solution (Beantown Chemical, Hudson, NH, USA) on plain microscope glass slides. The cells were then given a five-time PBS wash, a five-time double-distilled water wash, and a room-temperature air-drying period.

4.3 Instruments

The alpha 300RAS WITec system (WITec GmbH, Ulm, Germany) was used to acquire the confocal Raman images with scan sizes of 55 μm × 55 μm. This system consists of a microscope connected by an optical fiber with a core diameter of 50 μm to a triple grating monochromator/spectrograph and a thermoelectrically cooled Marconi CCD camera. The excitation of a frequency-doubled neodymium-doped yttrium-aluminum-garnet (Nd: YAG) laser

(λ = 532 nm) and a 50X air objective lens (Nikon, Tokyo, Japan) with a numerical aperture (NA) of 0.75 were used in the current measurements. The average laser power was kept at a small output of around 3 mW to prevent sample photodegradation. Surface Raman mapping images of untreated and NDGA-treated GBM cells were obtained using arrays of 150 × 150 Raman spectra, each with an integration duration of 500 ms. The confocal microscopic data was collected using the WITec Control program, which also operates the piezoelectric stage for sample scanning.

4.4 Computational Analysis

The MATLAB® version r2016a was used to implement an in-house algorithm in the current statistical analysis. A general linear background subtraction was applied to the Raman output data from 377 cm^{-1} to 3500 cm^{-1} before implementing the algorithm. All the spectra were normalized to the intensity of the laser line, whose height was derived from a Gaussian fit to maintain consistency between measurements of various samples and eliminate potential slight variations in the laser power during the quick confocal data recording. Additional linear background subtractions were also performed for the integrated regions under the important Raman features to increase the calculations' accuracy.

The specific frequency regions of this second background subtractions are as follows: for the phenylalanine vibrational line centered at 1004 cm^{-1}, from 980 to 1040 cm^{-1}; for the amide III convoluted features with centers at 1267 cm^{-1}, 1338 cm^{-1} (cancer sample), and 1304 cm^{-1} (non-cancerous sample), from 1190 to 1400 cm^{-1}; for the band with a central maximum at about 1461 cm^{-1} (lipid, protein), from 1400 to 1530 cm^{-1}; for the peak at 1667 cm^{-1} (amide I, -sheet) and the broadband centered at 1605 cm^{-1} (phenylalanine, decreased nicotinamide adenine

dinucleotide (NADH), tryptophan, mitochondria), from 1530 to 1750 cm^{-1}, respectively; and for the peaks centered at 2854 cm^{-1} (fatty acids, aliphatic acyl chain of endogenous lipids), 2888 cm^{-1} (lipids), and 2935 cm^{-1} (proteins), from 2800 to 3040 cm^{-1}, to incorporate these three convoluted features [16].

About 1000 spectra corresponding to cells were chosen for each sample to calculate the ratios of various parameters associated with compositional content changes. Even though calculations were individually done for all possible combinations of these parameter ratios for each spectrum, only the ratios demonstrating obvious patterns of the NDGA's effects are provided and addressed in the current study.

4.5 Raman Microscopic Investigations of NDGA Therapeutic Effects on GBM

To accurately identify morphological changes in GBM bio-signatures upon treatment with NDGA, knowledge of bio-signatures from benign and malignant biospecimens should be first achieved. In addition to performing a literature review of Raman spectroscopy potential for identifying cancerous biospecimens [25], we also experimentally acquired such data. The Raman spectra of normal (non-cancerous) and malignant (cancerous) control cell samples obtained from mouse brain tissue and GBM cancer cells, respectively, are first shown in Figure 4.1. These spectra demonstrate how fundamental changes in biochemical cell structure accompany pathological cell modification. Tens of thousands of gathered spectra were averaged to produce these two representative Raman spectra (90,000 for the current measurements). A break between 1800 and 2650 cm^{-1} was used to allow all of the regions of interest be incorporated into these spectra and to enable visual identification of variations vibrational signatures between these two control samples. Additionally, for more straightforward visualization and comparison the spectra

were translated vertically. The spectra in Figure 4.1 distinctively differentiate between specific vibrational lines' strengths corresponding to, biocomponents in either normal and cancerous samples, such as nucleic acids, lipids, and proteins. They also strongly agree with similar published findings in the literature [61][30].

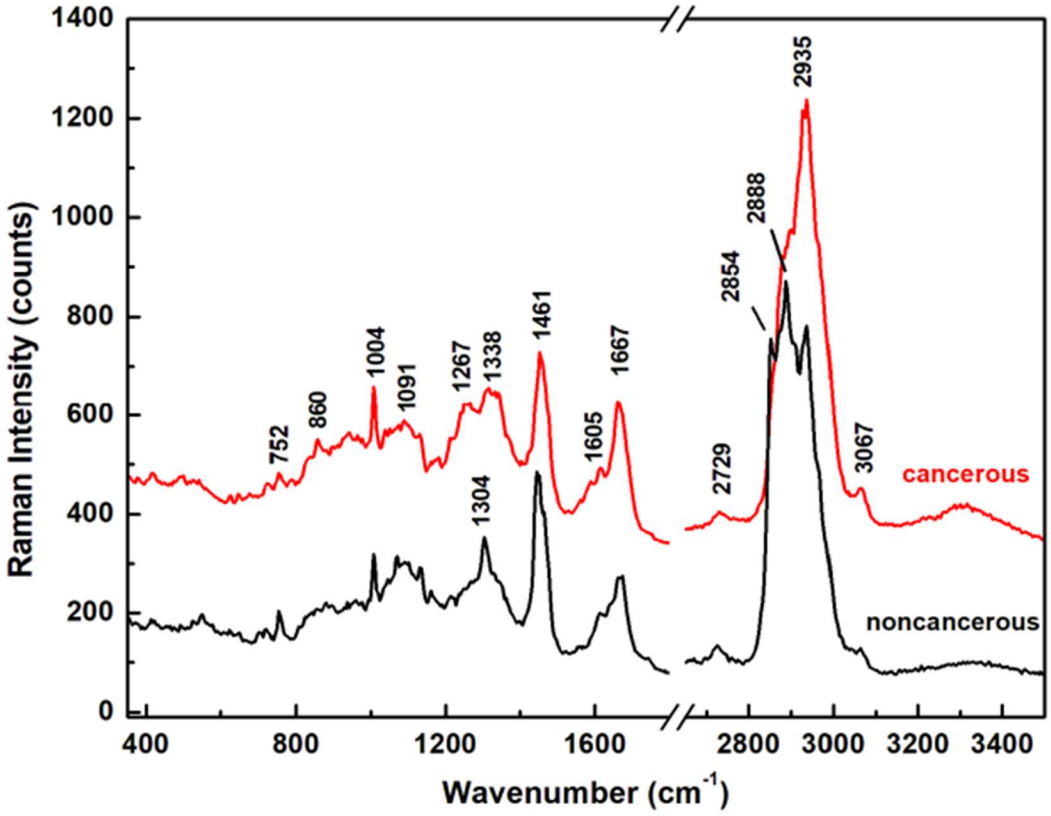

Figure 4.1 Integrated Raman spectra of the GBM cancer control sample (red spectrum) and the normal control sample (black spectrum). [16]

The 2800 – 3000 cm^{-1} lipid-protein profile region is where cancerous and noncancerous Raman spectra are most significantly different[61][30]. The Raman peak at 2935 cm^{-1}, which is noticeably stronger for the GBM malignant sample, indicates a more significant concentration of transformed protein. Amide I (β-sheet, cholesterol esters), responsible for the slight increase in the vibrational line intensity at 1667 cm^{-1} supports this result. The slight intensity decreases of the Raman signal at 1461 cm^{-1} is also related to a biochemical alteration in the structure of

proteins. Analysis and reports of these specific characteristics occurring in this spectroscopic region have already been published and correlated with primary indications of carcinogenesis [53][27].

On the other hand, the spectrum of the normal control sample, which has prominent Raman peaks at 2888 cm^{-1} and 2854 cm^{-1}, indicates a dominating lipid content (fatty acids, aliphatic acyl chain of endogenous lipids). These two Raman vibrational lines become only a wide shoulder in the low-frequency region of the 2935 cm^{-1} peak for the GBM sample. Therefore, the underlying cause of these observed structural alterations could be an abnormal lipid-protein metabolism, which is known to occur in a variety of cancers and have as outcome a post-translational modification of proteins [62][63].

Although not exclusively, it has been proposed that the overexpression of proteins and the deregulation of signaling pathways seen in cancer metabolism are caused mainly by changes of the cell membrane [62][63]. The apparent variations in phospholipid, protein amide III, nucleic acid, and collagen composition provide additional supporting evidence. For instance, in the spectrum associated with the normal control sample, the sharp, intense Raman peak at 1304 cm^{-1} (lipids, phospholipids, collagen, protein amide III, and DNA) splits into two broad, less intense Raman features at 1267 cm^{-1} (amide III, fatty acids, and P=O asymmetric stretch due to nucleic acids) and 1338 cm^{-1} (protein, DNA/RNA, tryptophan, and mitochondria) in the spectrum of the malignant sample.

The vibration at 1091 cm^{-1} (cell membrane phospholipids and nucleic acids) similarly broadens and loses strength. Additionally, a noticeable rise in the quantity of phenylalanine with structural changes of the cells toward a malignant configuration is associated with an amplification of the peak at 1004 cm^{-1}. Therefore, phenylalanine can be considered as a

biomarker of tumorigenesis, in addition to the ones mentioned above and already reported in the literature for malignant tumors, such as the observed abnormal lipid-protein metabolism, overexpression of amide I, and potential transformation of the α-helix structure into a β-sheet [61][30][57][62][63]. Table 4.1 below lists all the Raman vibrational bands detected in the spectra and their tentative attributions and assigned roles.

Table 4.1 tentative attributions for the Raman vibrational bands and their assignments. [16]

Raman Wavenumber cm^{-1}	Assignment [a,b]	Tentative Attribution [a,b]
752	CH_2 rocking, symmetric breathing	Tryptophan, cytochrome c, mitochondria [a] Nucleic acids, tryptophan [b]
860	CC stretch	Tyrosine, proline, glycogen [b]
1004	Symmetric CC aromatic ring breathing	Phenylalanine, collagen IV, I [a] Phenylalanine [b]
1091	CC skeletal stretch, PO_2 symmetric stretch	Protein, phospholipids, glycogen, collagen IV, I [a] Phospholipids, nucleic acids [b]
1267	Amide III, =C–H bend, P=O asymmetric stretch	Homo polypeptide [a], Fatty acids [b]
1304	Amide III, N–H bend, α-helix, C–N stretch, and CH_3 bend, C–H^2 twist	Bending and stretching coupled in-phase, collagen IV, I [a] Lipids, phospholipids, collagen, protein, DNA [b]
1338	CH_2 deformation	Protein, A and G of DNA/RNA [a] Tryptophan [b]
1461	CH_2 or CH_3 out-of-phase deformation, CN bend	Lipid, protein [a] Protein [b]
1605	Amide I α-helix, CO stretch, C=C bend	Protein, phenylalanine, tyrosine [a] Unsaturated fatty acids, triglycerides [b]
1667	Amide I β-sheet, C=O stretch	Unordered or random structure, collagen IV, I [a] Proteins, cholesterol esters [b]
2729	CH_3 in-phase deformation overtone	
2854	CH_2 symmetric stretch	Fatty acids, triglycerides [a,b]
2888	CH_2 asymmetric stretch	Lipids [a,b]
2935	CH_3 symmetric stretch	Proteins [a,b]
3067	CH_3–(C=O), C–H aromatic	Nucleic acids, proteins [b]

Following the primary goal of this analysis, to evaluate the role of NDGA in reducing malignant brain tumors, we display surface confocal Raman mapping images of an untreated (control) GBM sample and two NDGA-treated GBM samples in Figure 4.2 a, c, e, respectively. Figure 4.2 b, d, and f display the matching spectroscopic data for each image (average of 22,500 individual spectra recorded per image). For the two individually treated samples, concentrations of 100 μM NDGA and 250 μM NDGA were applied for 24 and 4 hours, respectively.

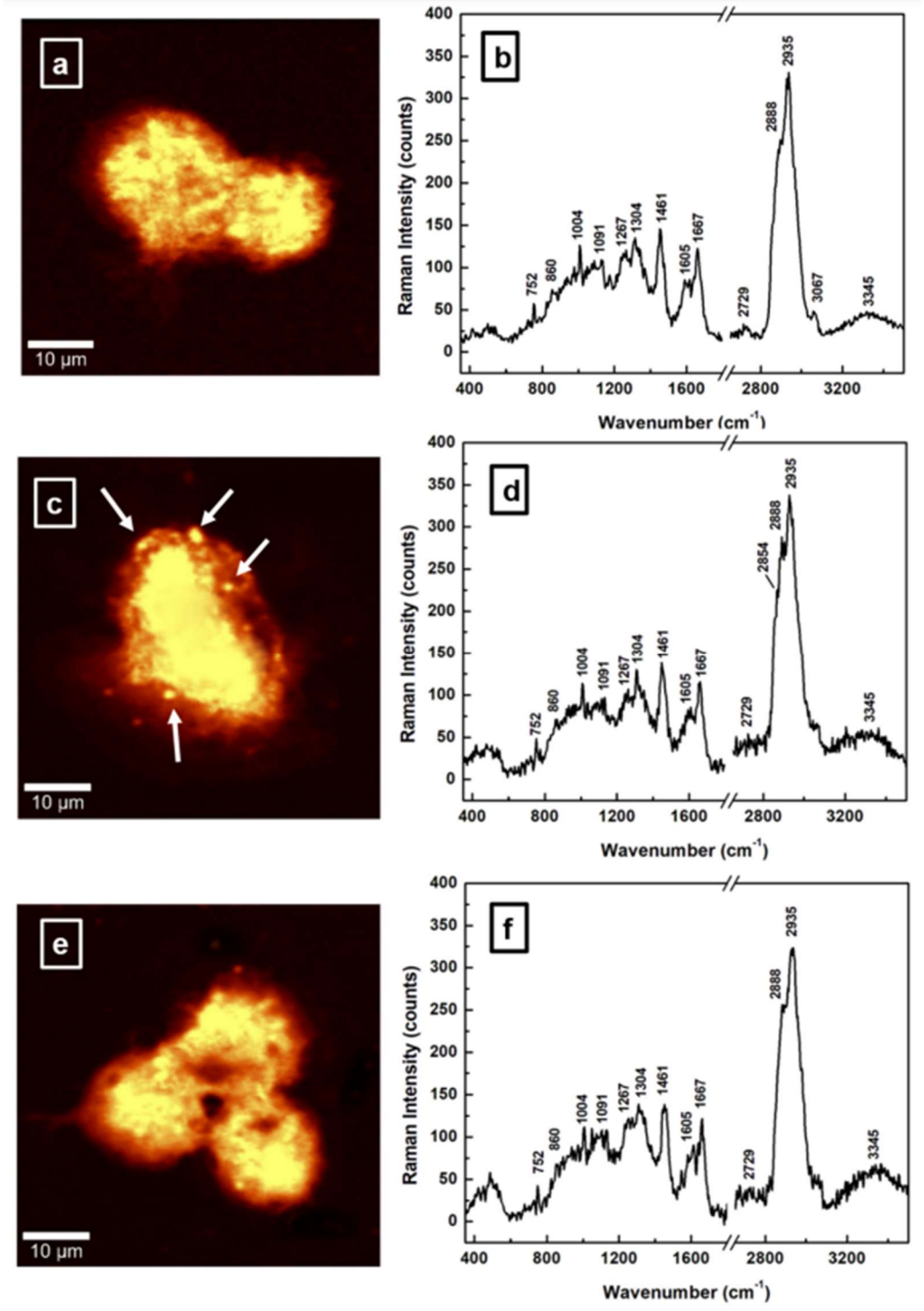

Figure 4.2 Representative photos of surface confocal Raman mapping of; **(a)** untreated (control) GBM cells, **(c)** 100 µM NDGA-treated GBM sample treated for 24 h, and **(e)** 250 µM NDGA treated GBM sample treated for 4 h. Brighter yellow pseudo-colors have higher intensities. **(b, d, f)** Raman spectra are associated with each image and only in vibrational regions of interest. [16]

For a straightforward comparison with the Raman bio-structural signatures shown in Figure 4.1, the same frequency regions were considered with a break between 1800 and 2650 cm-1 in the spectra presented in Figure 4.2b, d, and f. Additionally, background subtraction and normalization to the 2935 cm^{-1} vibrational line's intensity were conducted. At these low NDGA concentration levels, which are below the threshold of Raman spectroscopy detectability, direct detection of NDGA is not expected to be possible. However, NDGA treatment is anticipated to cause structural modifications to the cell. Therefore, by detecting these modifications, we can investigate some of the molecular processes of the NDGA treatments, which are essential for the possibility of its therapeutic application.

The ratio of protein-to-lipid content, determined by the I_{2935}/I_{2888} intensity ratio of the relevant Raman features, decreases in the integrated spectrum of the untreated sample (GBM control sample, Figure 4.2b) compared with this value for the NDGA-treated samples (Figure 4.2d, f). The malignant GBM sample yields a value of 1.32 ± 0.03; the NDGA-treated GBM sample treated with 100 μM for 24 hours produces a value of 1.20 ± 0.03; and the NDGA-treated GBM sample treated with 250 μM for 4 hours yields a value of 1.26 ± 0.03. Since the I_{2935}/I_{2888} ratio is anticipated to be lower for the normal control sample at about 0.87 ± 0.03, the decrease in the amount of acetylated protein suggests that NDGA is beneficial.

The existence of the lipid droplets shown by white arrows in Figure 4.2c, which correspond spectroscopically to the very weak feature at around 2854 cm^{-1} for the sample treated with 100 μM NDGA, provides additional proof that NDGA influences the cell's lipid-protein metabolism (see Figure 4.2d). On the other hand, Figure 4.2f, shows a lipid peak at 2888 cm^{-1} for a higher dose of NDGA administered over a shorter period (like bolus therapy). This feature is somewhat more prominent than in the Raman spectrum of the GBM sample (Figure

4.2b). In addition to showing less evidence of lipid droplets, a closer examination of the image and the Raman spectrum shown in Figures 4.2e, and f, respectively, demonstrates an increase in fatty acid content, which is also a sign of altered metabolism in cancer (note the slightly higher intensity of the 1267 cm^{-1} line) [30]. It was concluded that the Otto-Warburg effect causes this de novo fatty-acid production. A consequence of increased glucose catabolism is an increase in pyruvate as a byproduct, which is then transformed into lactate and acetyl coenzyme A (acetyl-CoA) [30]. The latter is a recognized element in biochemical processes involving carbohydrates and lipid-protein metabolism. More importantly, a higher NDGA dose is toxic and causes cell membrane damage and apoptosis (see Figure 4.2e).

The transformation of the α-helix structure into β-sheet and the overexpression of amide I are two more structural modifications [57]. The I_{1667}/I_{1605} intensity ratio of the associated Raman bands is considered. Values of 1.35 ± 0.03 for the normal control sample, 1.49 ± 0.03 for the GBM tumorigenic sample, 1.45 ± 0.03 for the NDGA-treated GBM sample treated with 100 μM for 24 hours, and 1.47 ± 0.03 for the NDGA-treated GBM sample treated with 250 μM for 4 hours are estimated here. These results indicate that NDGA addition does not significantly reverse the undesirable structural transformation linked to the tumorigenic samples.

Analysis of the intensity of the phenylalanine vibrational line reveals a decrease from the untreated GBM sample to the NDGA-treated samples. Results showed that the GBM tumorigenic sample had a value of 38.2 ± 0.02, the NDGA-treated sample had a value of 37.5 ± 0.02 after being exposed to 100 μM for 24 hours, the NDGA-treated GBM sample had a value of 29.7 ± 0.03 after being exposed to 250 μM for 4 hours, and the normal control sample had a value of 28.5 ± 0.02. Phenylalanine, an important amino acid, is typically obtained from the diet and biologically converted into tyrosine. Unfortunately, ROS-damaged phenylalanine also

occurs in malignant tumors [64]; this fact is supported by the visible increase of the 1004 cm^{-1} vibration line for the cancerous sample in Figure 4.1. It is still not clear how exactly these amino acids with ROS damage enter proteins and alter their structure. They could, however, have an impact on the increase of the 2935 cm^{-1} peak in Figure 4.1. Based on the data, NDGA, a ROS scavenger and antioxidant phenolic lignan, reduces and eliminates such ROS-damaged phenylalanine production.

Figures 4.3 and 4.4 provide a more condensed and informal representation of the possible advantageous effect of NDGA in lowering some of the elements linked to cell malignancy.

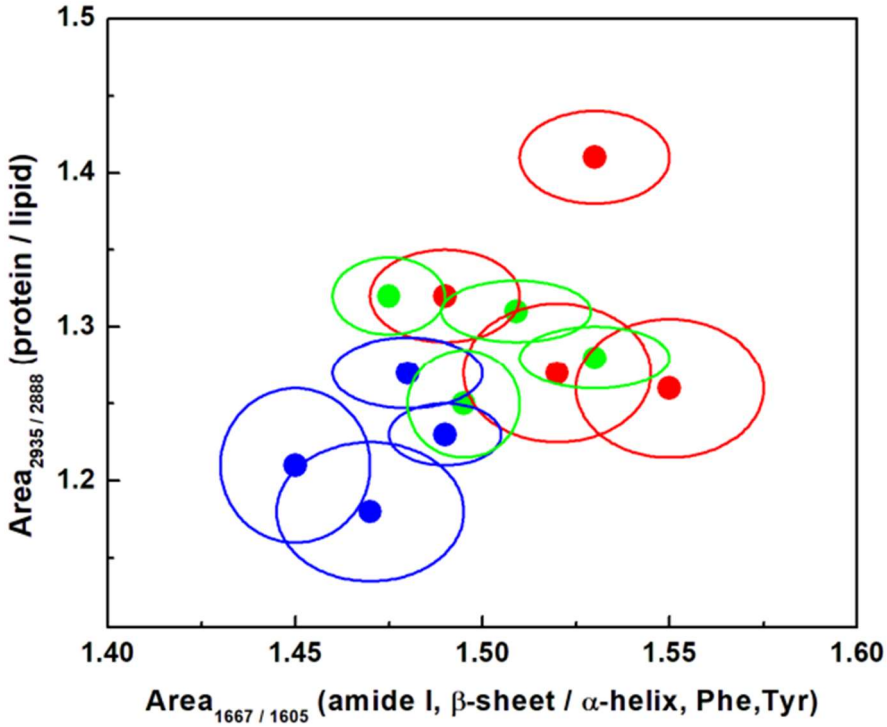

Figure 4.3 The content ratios for the protein to lipid contents (i.e., ratios of 2935 cm-1 to 2888 cm-1), and the protein, amide I sheet, phenylalanine, and tyrosine contents (i.e., ratios of 1667 cm-1 to 1605 cm-1) are statistically represented using 1-sigma ellipsoids. For each biomarker, the average of over 22,500 spectra is defined by the solid circle. The malignant GBM sample is represented by a red color code, blue for the NDGA-treated GBM sample that had been exposed to 100 μM for 24 hours, and green for the NDGA-treated GBM sample that had been exposed to 250 μM for 4 hours.[16]

The averages of the compound content across all spectra are represented statistically by the solid circles in the 1-sigma ellipsoid representations. This representation also makes it possible to identify anticipated variations among the same type of samples. To reduce calculation errors caused by sample roughness and inhomogeneity, and to eliminate the influence of polarization-sensitive effects of certain elements, the integrated areas beneath the peaks are considered rather than their intensities. Figure 4.3 shows the relationship between the protein-to-lipid content ratio, A_{2935}/A_{2888}, and the A_{1667}/A_{1605} protein, amide I -sheet, phenylalanine, and tyrosine. In addition to agreeing with our earlier observation that administering NDGA positively impacts lowering the quantity of modified protein content, inter-sample variance is also visible.

The signal-to-noise (S/N) ratio rise in the spectra shown in Figure 4.2d and f, which is the first indication of the increase in cell fluorescence with NDGA integration, impacts the measurements and increases the errors in differentiating between the samples. However, based on the current findings, a smaller NDGA dose of 100 μM NDGA for 24 hours is recommended, not only because it may have reduced toxicity but also because it allows for greater sample differentiation (comparison between 1-sigma ellipsoid blue color plots and those of red color).

Another point worth highlighting is the anticipated auto-oxidation of NDGA itself and its transition into semi-quinone or ortho-quinone forms, which have vibrational frequencies in the 1600 cm^{-1} range [19][47]. Less differentiation between the samples for A_{1667}/A_{1605} is anticipated since a greater quantity of NDGA incorporation would result in a greater number of these oxidized species (comparison of 1-sigma ellipsoids along the horizontal axis).

Figure 4.4 shows statistical charts comparing the ratio of the amount of phenylalanine to the total amount of proteins and lipids ($A_{1004}/A_{2935+2888}$) to the ratio of changes of lipid and protein biostructures ($A_{2888}/A_{2935+1461}$).

With even worse toxicological effects than NDGA, lipid-lowering and anti-lipid peroxidation therapies have been investigated for other anticancer drugs. As a result, the examination of Figure 4.4 can offer detailed insights into how NDGA affects the molecular mechanism linking lipid metabolism to cancer and the inhibition of ROS-damaged phenylalanine formation.

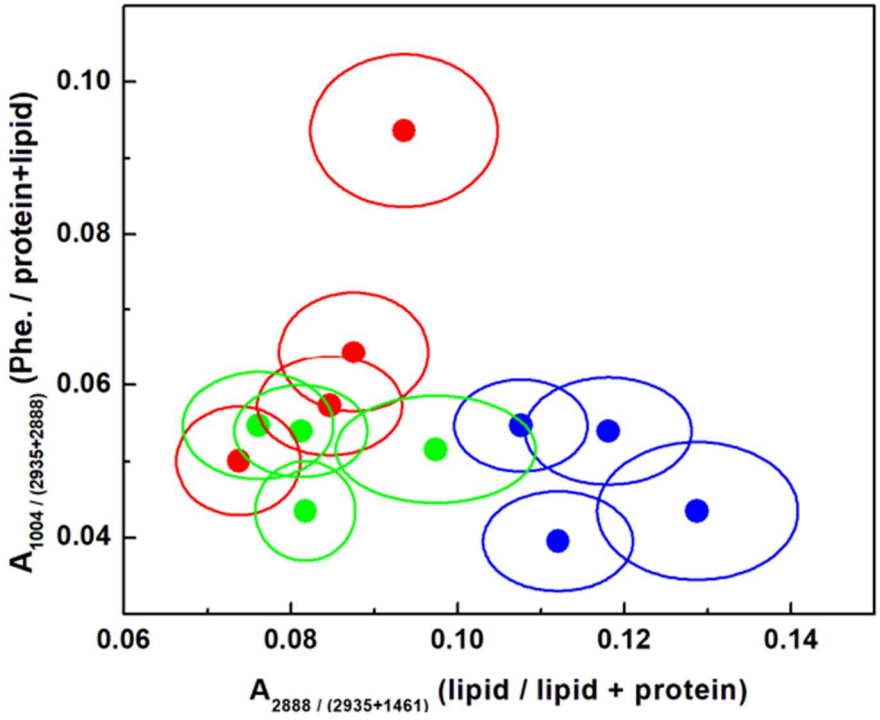

Figure 4.4 Using 1-sigma ellipsoids, a statistical representation of the ratios of phenylalanine to combined protein and lipid content (i.e., ratios of peak areas at 1004 cm1 to corresponding sums obtained by adding peak areas at the 2935 cm1 and 2888 cm1) and the corresponding ratios of lipid to overall protein content (i.e., ratios of peak areas at 2888 cm1 to corresponding sums obtained by adding peak areas at 2935 cm1 and 1461 cm1). The solid circle depicts the average of approximately 22,500 spectra for each biomarker. Red was utilized to indicate a malignant GBM sample, blue for NDGA-treated GBM samples that were given 100 µM for 24 hours, and green for NDGA-treated GBM samples that were given 250 µM for 4 hours. [16]

While the trend along the vertical axis for both NDGA concentrations shows a decrease in the ROS-damaged phenylalanine, the direction along the horizontal axis indicates that NDGA administration at a higher dosage results in less lipid development. This latter observation confirms our earlier finding that cells treated with 100 μM NDGA for 24 hours developed more lipid droplets than cells treated with a higher dosage of 250 μM for 4 hours (see Figure 4.2c). It is also important to consider the potential structural cell damage caused by NDGA's cytotoxicity at larger dosages.

We used principal component analysis (PCA) to assess the experiments' capacity further in distinguishing between untreated and NDGA-treated cells. When completing the PCA, all the measured Raman vibrational lines and their ratios were considered variables. A benefit of using PCA is that it does not account for the spectra's general classification, which prevents the introduction of bias based on past information. To enhance the visualization of the results shown in Figure 4.5, the system's dimensionality was reduced.

About 78% of the variation across all samples is included in the first two principal components. Additionally, a similar color-coding system was employed to maintain consistency with the data of earlier figures, with red designating GBM samples, blue designating NDGA-treated GBM samples treated with 100 μM for 24 hours, and green designating NDGA-treated GBM samples treated with 250 μM for 4 hours. The primary finding of this graph is the separation of the data point clusters for the three different sample types, with some overlap between the untreated GBM and the NDGA-treated with 100 μM samples. For sample classification, Linear Discriminant Analysis (LDA) was utilized.

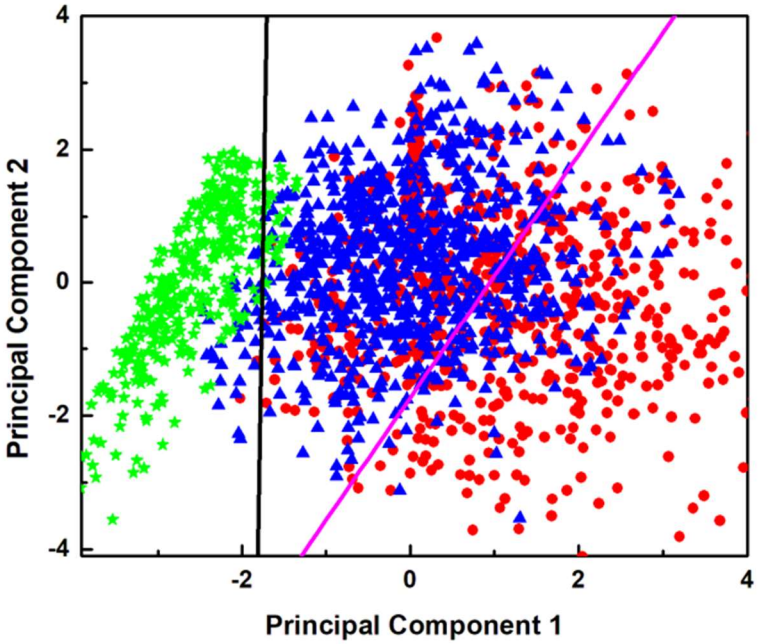

Figure 4.5 Principal component analysis (PCA) demonstrates a distinct division between the data point clusters of the samples. For consistency, the malignant GBM sample, the NDGA-treated GBM sample treated with 100 M for 24 hours, and the NDGA-treated GBM sample treated with 250 M for 4 hours, respectively, all employed the same color codes of red, blue, and green. [16]

Because a dosage of more than 100 μM NDGA has been reported as toxic, we undertook additional testing using machine-learning approaches to construct a completely automated framework that makes choices directly from the Raman spectra provided as input. We used all the ratios as variables of the input training for different statistical learning algorithms to better discriminate between cell samples. Statistical learning algorithms used were Support Vector Machines (SVM), k-Nearest Neighbor (kNN), Decision Tree Learning (DTL), and "Nave Bayes Classifiers" (NBC), using five-fold cross-validation. All of these statistical learning techniques led to a classification accuracy of approximately 80%. Table 4.2 below provides the confusion matrix for the Linear Support Vector Machine (LSVM).

Table 4.2 Accuracy using LSVM with 5-fold cross-validation. [16]

		Predicted		
		Untreated GBM	100 µM NDGA-Treated	250 µM NDGA-Treated
True	Untreated GBM	68.2%	31.8%	0%
	100 µM NDGA-treated	16.8%	81.2%	2.0%
	250 µM NDGA-treated	0 %	4.8%	95.2%

According to the table, the algorithm correctly identified a single spectrum (true positive) in 68.2% of untreated GBM samples, 81.2% of samples treated with 100 µM NDGA, and 95.2% of samples treated with 250 µM NDGA. Additionally, it revealed a 31.8% misclassification in classifying the untreated GBM samples as those treated with 100 µM NDGA. In the samples treated with 100 µM NDGA, 2.0% are misclassified as treated with 250 µM NDGA and 16.8% as untreated GBM. The 250 M NDGA-treated samples are divided more clearly, and no such incorrect untreated categorization is made; just 4.8% are misclassified as having had 100 µM NDGA treatment. These findings support those depicted in Figure 4.5. They further indicate that accurate sample discrimination requires using many spectra, not just one.

The simultaneous recording of multiple spectra from the same sample is one of the benefits of Raman microscopy, which may be seen as independent sampling from the viewpoint of statistics (each spectrum is recorded at a slightly different position). The probability of misclassification is given by the following equation 4.1, assuming that p is the true positive rate and (1-p) the false-negative rate, where k is the number of spectra that are not connected with a category (0<k<N/2) and N is the total number of independent spectra that were measured from the same sample.

$$Q(N) = 1 - \sum_{k=0}^{k<\frac{N}{2}} \binom{N}{k} (p)^{N-k}(1-p)^{k} \tag{4.1}$$

Figure 4.6 provides these probabilities for sample misclassification following N Raman recordings. Two horizontal lines indicating the error probability of p = 0.05 and p = 0.01 are included in this image to help visualize the measurements necessary to categorize the samples properly.

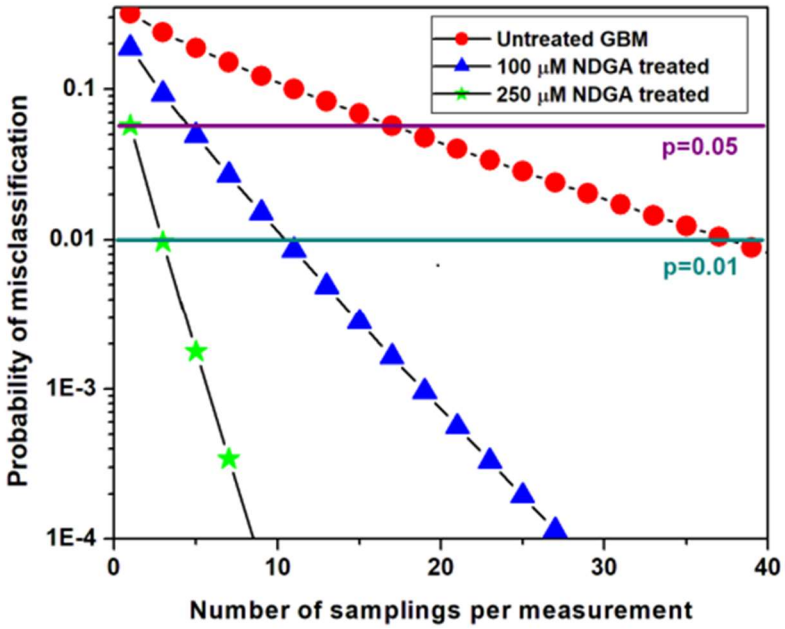

Figure 4.6 The probability of classification error vs. the number of randomly selected spectra used in the classification. The vertical dark cyan and violet lines are used to more easily visualize the sets of measured spectra needed to categorize the samples with error probabilities of 0.05 and 0.01, respectively.[16]

A 95% accuracy classification of the samples may be made with around 21 spectra, while a 99% accuracy classification requires 41 spectra. These figures are incredibly small compared to the 10,000 independent spectra per sample that confocal Raman microscopy can provide. In addition to having very high a classification accuracy, the Raman approach also offers the potential for future in vivo applications.

CHAPTER 5

CONCLUSIONS AND FUTURE WORK

5.1 Concluding Remarks on NDGA

As a potent ROS scavenger, NDGA has demonstrated promising relevance in treating several disorders, including cancer, cardiovascular, renal, pulmonary, neurological, and a wide range of viruses [19]. We theoretically and experimentally evaluate this molecule using DFT calculations, Raman spectroscopy, and FTIR spectroscopy, to optically provide new insights into which NDGA morphological conformation offers health advantages, and which one harms. We have successfully identified the vibrational signals of different NDGA structural variations linked to its chemical oxidation changes. The assigned signatures are as follows: Raman 790 cm^{-1} and IR 1190 cm^{-1} for neutral NDGA, Raman 1337 cm^{-1} and IR 1159 cm^{-1} for para-quinone NDGA, Raman 1583 cm^{-1} and IR 1663 cm^{-1} for ortho-quinone NDGA, and Raman 1581 cm^{-1} IR and 1663 cm^{-1} together with disappearance of the 790 cm^{-1} for fully oxidized NDGA. In addition to the contribution of orthoquinone, the current findings suggest that the fully oxidized form is more likely to accumulate and produce in vivo toxicity.

More studies must be done concerning a more complicated biological environment. The current spectroscopic analysis gives some necessary scientific background for understanding the changes in the vibrational signatures of this significant bio-medicinal, plant-derived compound. This is important if the future development of new drugs and their successful implementation is anticipated. Knowing that high concentrations of NDGA can be toxic, we examine next its efficacy as a bolus therapeutic method (high concentration over short periods) or a quasi-metronomic (lower concentrations over a more extensive period).

5.2 Concluding Remarks of NDGA's Therapeutic Effects on GBM

The main objective is to show that Raman microscopy could be used to detect structural variations in GBM cells before and after treatment with NDGA. This information will help researchers better understand the compound's ability to alleviate brain tumors. In addition to the experimental Raman analysis, the computational strategy enables a more accurate distinction between benign and malignant brain tumor biospecimens , as well as minute structural alterations in GBM's bio-signatures after NDGA administration. Thus, to properly understand the significance of NDGA in GBM therapeutics, a previous analysis of the main vibrational signatures that help discriminate between normal and malignant samples was considered significant. Results derived from this study suggest that NDGA positively affects altered protein content and ROS-damaged phenylalanine levels. It is worth noting that phenylalanine, along with other well-known cancer biomarkers, may be used to classify samples and determine the efficiency of NDGA. We have been proven here that administering NDGA in repeated, lower doses over a more extended period is a more effective therapeutic strategy, much like a quasi-metronomic therapy.

Another significant finding concerns the abnormal lipid-protein metabolism connected to different cancer types and the formation of lipid droplets. Once more, it is advised to use a lower NDGA dosage during treatment, since very high dosages of NDGA can destroy cell membranes and other structural components, acting almost like chemotherapy. If used as a bolus treatment, the well-known harmful cytotoxicity of NDGA in large doses could have some positive chemotherapeutic benefits. This assumption should be assessed. It is also necessary to determine how well other potential NDGA chemical derivatives operate in therapeutic settings. Fast acquisition of random Raman spectra numbering about 100 is planned for evaluating the number

of occasions in which the NDGA-treated and untreated samples would be found statistically significantly different (at the $p = 0.05$ level), moving us closer to potential in vivo implementation of our spectroscopic method and our statistical algorithm in assessing GBM as a disease.

5.3 Future Work

This research provides the basis and knowledge of NDGA's advantageous and disadvantageous mechanisms of action necessary for developing effective brain cancer treatments. We predict that new therapeutic development will advance continuously and more effectively if our findings are compared to further in vivo investigations of NDGA's bioactivity. In the future, we want to do a double-blind study on such samples utilizing our algorithm, the Raman technique, and complementing standard bioanalysis independently to compare the outcomes of both strategies**.**

The study accomplished here only focused on aggressive glioblastoma multiforme, such as GBM6. Thus, investigations of other less aggressive forms, such as GMB1 or GBM2, should also be studied. The study showed a reduced amount of altered lipids and proteins in GBM6; it would be interesting to investigate if NDGA has an increased or decrease effect in less aggressive forms of cancer. Other cancer cell lines should also be analyzed using the same approach used in this study. Due to the different biological environments, NDGA could potentially have a different therapeutic effect on various cancer cell lines.

Another point of interest lies in the number of different conformations of NDGA can have. Based on the ability to scavenge free radicals or ROS of the molecule, investigations regarding the scavenging efficiency for different conformations of the antioxidant should be

pursued. Some mechanisms of NDGA's OH radical scavenging activity have been studied [51]. However, studies regarding the effects of different conformation in more complex biological environments are yet to be accomplished.

Regarding the Creosote bush itself, around thirty genera exist, and about 250 species live in the Zygophyllaceae family [65]. Considering the many therapeutic effects of *Larrea Tridentata*, other plants of its family should also be considered for investigation. Botanists now know that the species of creosote they had thought existed in the deserts of North America are made-up of three genetically distinct bushes. The creosote bushes of the Mojave Desert have 78 chromosomes, the Sonoran Desert (in southern Arizona) has 52, and the Chihuahuan Desert in west Texas has just 26 [7]. The capacity to survive in the Mojave Desert's dry summers may have increased along with the number of chromosomes. It is interesting to know if the number of chromosomes affects the number of oils the bush produces. Because the plant uses the oils in the leaves to protect itself from pests and fungus, together with the fact that NDGA is mostly found in the leaves, it will be interesting to investigate if the number of chromosomes affects its therapeutic effects when consumed as an herbal tea.

Overall, the Creosote bush and NDGA hold great promise for future therapeutic applications based on this study. NDGA is known to have a therapeutic effect on many diseases, and only a few are just beginning to be studied. Only the surface of the potential of NDGA is uncovered.

REFERENCES

[1] H. Yuan, Q. Ma, L. Ye, and G. Piao, "The Traditional Medicine and Modern Medicine from Natural Products," *Molecules*, vol. 21, no. 5, p. 559, Apr. 2016, doi: 10.3390/molecules21050559.

[2] M. Serafini, D. del Rio, D. N. Yao, S. Bettuzzi, and I. Peluso, *Health Benefits of Tea*. 2011. [Online]. Available: http://www.ncbi.nlm.nih.gov/pubmed/22593935

[3] S.-Y. Pan *et al.*, "Tea and tea drinking: China's outstanding contributions to the mankind," *Chin Med*, vol. 17, no. 1, p. 27, Dec. 2022, doi: 10.1186/s13020-022-00571-1.

[4] N. Khan and H. Mukhtar, "Tea and Health: Studies in Humans," *Curr Pharm Des*, vol. 19, no. 34, pp. 6141–6147, Sep. 2013, doi: 10.2174/1381612811319340008.

[5] "From immune function and cognition to cardiovascular health and cancer prevention - health benefits of tea revealed by researchers from across the globe.," *NewsRx Health & Science*, no. Gale OneFile: Contemporary Women's Issues, p. 166, 2022, [Online]. Available: https://go.gale.com/ps/i.do?p=CWI&u=txshracd2603&id=GALE%7CA702850369&v=2.1&it=r&sid=bookmark-CWI&asid=73388729

[6] I. F.F. Benzie and S. Wachtel-Galor, "Health Benifits of Tea," in *Herbal Medicine, 2nd edition Biomolecular and Clinical Aspects*, 2011.

[7] H. DeLisle, "Creosote Bush," *National Park Service*, 2015.

[8] S. Arteaga, A. Andrade-Cetto, and R. Cárdenas, "Larrea tridentata (Creosote bush), an abundant plant of Mexican and US-American deserts and its metabolite nordihydroguaiaretic acid," *J Ethnopharmacol*, vol. 98, no. 3, pp. 231–239, Apr. 2005, doi: 10.1016/j.jep.2005.02.002.

[9] "Creosote Bush," *Earth Observatory Nasa*. https://earthobservatory.nasa.gov/biome/seedcreosote.php

[10] "larrea tridentata," *wikipedia*, 2022. https://en.wikipedia.org/wiki/Larrea_tridentata

[11] S. Heron and E. Yarnell, "The Safety of Low-Dose Larrea tridentata (DC) Coville (Creosote Bush or Chaparral): A Retrospective Clinical Study," *The Journal of Alternative and Complementary Medicine*, vol. 7, no. 2, pp. 175–185, Apr. 2001, doi: 10.1089/107555301750164262.

[12] C. W. Waller and O. Gisvold, "A phytochemical Investigation of Larrea Divaricata Cav.*," *Journal of the American Pharmaceutical Association (Scientific ed.)*, vol. 34, no. 3, pp. 78–81, Mar. 1945, doi: 10.1002/jps.3030340305.

[13] E. Floriano-Sánchez *et al.*, "Nordihydroguaiaretic acid is a potent in vitro scavenger of peroxynitrite, singlet oxygen, hydroxyl radical, superoxide anion and hypochlorous acid

and prevents in vivo ozone-induced tyrosine nitration in lungs," *Free Radic Res*, vol. 40, no. 5, pp. 523–533, Jan. 2006, doi: 10.1080/10715760500419365.

[14] F. S. Manciu *et al.*, "Comparative spectroscopic analysis of nordihydroguaiaretic acid and related natural products to inhibition of calcium oxalate calculi," *Biointerface Res Appl Chem*, vol. 9, no. 3, 2019, doi: 10.33263/BRIAC93.942948.

[15] K. Kimura and R. C. C. Huang, "Tetra-O-Methyl Nordihydroguaiaretic Acid Broadly Suppresses Cancer Metabolism and Synergistically Induces Strong Anticancer Activity in Combination with Etoposide, Rapamycin and UCN-01," *PLoS One*, vol. 11, no. 2, p. e0148685, Feb. 2016, doi: 10.1371/journal.pone.0148685.

[16] F. S. Manciu *et al.*, "Assessing Nordihydroguaiaretic Acid Therapeutic Effect for Glioblastoma Multiforme," *Sensors*, vol. 22, no. 7, p. 2643, Mar. 2022, doi: 10.3390/s22072643.

[17] S. Nusrat *et al.*, "A Comprehensive Spectroscopic and Computational Investigation to Probe the Interaction of Antineoplastic Drug Nordihydroguaiaretic Acid with Serum Albumins," *PLoS One*, vol. 11, no. 7, p. e0158833, Jul. 2016, doi: 10.1371/journal.pone.0158833.

[18] A. Galano, N. A. Macías-Ruvalcaba, O. N. Medina Campos, and J. Pedraza-Chaverri, "Mechanism of the OH Radical Scavenging Activity of Nordihydroguaiaretic Acid: A Combined Theoretical and Experimental Study," *J Phys Chem B*, vol. 114, no. 19, pp. 6625–6635, May 2010, doi: 10.1021/jp912001c.

[19] G. Manda, A. I. Rojo, E. Martínez-Klimova, J. Pedraza-Chaverri, and A. Cuadrado, "Nordihydroguaiaretic Acid: From Herbal Medicine to Clinical Development for Cancer and Chronic Diseases," *Front Pharmacol*, vol. 11, Feb. 2020, doi: 10.3389/fphar.2020.00151.

[20] H. Zhang, W.-J. Shen, Y. Cortez, F. B. Kraemer, and S. Azhar, "Nordihydroguaiaretic acid improves metabolic dysregulation and aberrant hepatic lipid metabolism in mice by both PPARα-dependent and -independent pathways," *American Journal of Physiology-Gastrointestinal and Liver Physiology*, vol. 304, no. 1, pp. G72–G86, Jan. 2013, doi: 10.1152/ajpgi.00328.2012.

[21] E. M. Ward *et al.*, "Annual Report to the Nation on the Status of Cancer, Featuring Cancer in Men and Women Age 20–49 Years," *JNCI: Journal of the National Cancer Institute*, vol. 111, no. 12, pp. 1279–1297, Dec. 2019, doi: 10.1093/jnci/djz106.

[22] A. C. Obenauf and J. Massagué, "Surviving at a Distance: Organ-Specific Metastasis," *Trends Cancer*, vol. 1, no. 1, pp. 76–91, Sep. 2015, doi: 10.1016/j.trecan.2015.07.009.

[23] D. X. Nguyen, P. D. Bos, and J. Massagué, "Metastasis: from dissemination to organ-specific colonization," *Nat Rev Cancer*, vol. 9, no. 4, pp. 274–284, Apr. 2009, doi: 10.1038/nrc2622.

[24] J. Fares, M. Y. Fares, H. H. Khachfe, H. A. Salhab, and Y. Fares, "Molecular principles of metastasis: a hallmark of cancer revisited," *Signal Transduct Target Ther*, vol. 5, no. 1, p. 28, Dec. 2020, doi: 10.1038/s41392-020-0134-x.

[25] M. Jermyn *et al.*, "Raman spectroscopy detects distant invasive brain cancer cells centimeters beyond MRI capability in humans," *Biomed Opt Express*, vol. 7, no. 12, p. 5129, Dec. 2016, doi: 10.1364/BOE.7.005129.

[26] J. Hernández-Damián, A. C. Andérica-Romero, and J. Pedraza-Chaverri, "Paradoxical Cellular Effects and Biological Role of the Multifaceted Compound Nordihydroguaiaretic Acid," *Arch Pharm (Weinheim)*, vol. 347, no. 10, pp. 685–697, Oct. 2014, doi: 10.1002/ardp.201400159.

[27] R. Wisastra and F. Dekker, "Inflammation, Cancer and Oxidative Lipoxygenase Activity are Intimately Linked," *Cancers (Basel)*, vol. 6, no. 3, pp. 1500–1521, Jul. 2014, doi: 10.3390/cancers6031500.

[28] I. Ivanov, H. Kuhn, and D. Heydeck, "Structural and functional biology of arachidonic acid 15-lipoxygenase-1 (ALOX15)," *Gene*, vol. 573, no. 1, pp. 1–32, Nov. 2015, doi: 10.1016/j.gene.2015.07.073.

[29] S. Fulda, A. M. Gorman, O. Hori, and A. Samali, "Cellular Stress Responses: Cell Survival and Cell Death," *Int J Cell Biol*, vol. 2010, pp. 1–23, 2010, doi: 10.1155/2010/214074.

[30] H. Abramczyk and A. Imiela, "The biochemical, nanomechanical and chemometric signatures of brain cancer," *Spectrochim Acta A Mol Biomol Spectrosc*, vol. 188, pp. 8–19, Jan. 2018, doi: 10.1016/j.saa.2017.06.037.

[31] D. R. Vij, Ed., *Handbook of Applied Solid State Spectroscopy*. Boston, MA: Springer US, 2006. doi: 10.1007/0-387-37590-2.

[32] Tsemii, "File:Raman scattering.svg," 2007. https://commons.wikimedia.org/wiki/File:Raman_scattering.svg

[33] N. Colthup B., S. Wiberley E., and L. Daly H., Eds., *Introduction To Infrared and Raman Spectroscopy*, 2nd ed. New York: Academic press, Inc., 1975.

[34] D. J. Gardiner and P. R. Graves, Eds., *Practical Raman Spectroscopy*. Berlin, Heidelberg: Springer Berlin Heidelberg, 1989. doi: 10.1007/978-3-642-74040-4.

[35] T. H. Kauffmann, N. Kokanyan, and M. D. Fontana, "Use of Stokes and anti-Stokes Raman scattering for new applications," *Journal of Raman Spectroscopy*, vol. 50, no. 3, pp. 418–424, Mar. 2019, doi: 10.1002/jrs.5523.

[36] N. Jaggi and D. R. Vij, "FOURIER TRANSFORM INFRARED SPECTROSCOPY," in *Handbook of Applied Solid State Spectroscopy*, Boston, MA: Springer US, pp. 411–450. doi: 10.1007/0-387-37590-2_9.

[37] M. Zitnik, Mimoza, and Neseska, “Fourier trasform infrared spectroscopy,” in *Fourier Transform Infrared Spectroscopy*, 2016, pp. 1–11.

[38] “An Introduction to the Fundamentals of FTIR Spectroscopy,” *Agilent* .

[39] N. Mimoza, “Fourier Transform Infrared Spectroscopy,” pp. 1–11, 2016.

[40] BWTek A Metrohm Group Company, “Introduction to Raman Spectroscopy”.

[41] G. S. Bumbrah and R. M. Sharma, “Raman spectroscopy – Basic principle, instrumentation and selected applications for the characterization of drugs of abuse,” *Egypt J Forensic Sci*, vol. 6, no. 3, pp. 209–215, Sep. 2016, doi: 10.1016/j.ejfs.2015.06.001.

[42] “What is confocal Raman Microscopy,” *Edinburgh Instruments* , 2023.

[43] Fausto D’Apuzzo, “Materials for Infrared and TeraHertz Plasmonics,” Sapienza Universita di Roma, 2015.

[44] N. P. Armitage, “Electrodynamics of correlated electron systems: Lecture Notes 2008 Boulder summer school on condensed matter physics,” 2008.

[45] S. A. Khan, S. B. Khan, L. U. Khan, A. Farooq, K. Akhtar, and A. M. Asiri, “Fourier Transform Infrared Spectroscopy: Fundamentals and Application in Functional Groups and Nanomaterials Characterization,” in *Handbook of Materials Characterization*, Cham: Springer International Publishing, 2018, pp. 317–344. doi: 10.1007/978-3-319-92955-2_9.

[46] M. Aamir Iqbal, N. Ashraf, W. Shahid, D. Afzal, F. Idrees, and R. Ahmad, “Fundamentals of Density Functional Theory: Recent Developments, Challenges and Future Horizons,” in *Density Functional Theory - Recent Advances, New Perspectives and Applications*, IntechOpen, 2022. doi: 10.5772/intechopen.99019.

[47] F. S. Manciu, J. Guerrero, D. Rivera, S.-Y. Chang, and K. Bennet, “Combined Theoretical and Experimental Study of Nordihydroguaiaretic Acid – From Traditional Medicine to Modern Spectroscopic Research,” *Biointerface Res Appl Chem*, vol. 10, no. 6, pp. 6728–6743, May 2020, doi: 10.33263/BRIAC106.67286743.

[48] A. D. Becke, “Density-functional thermochemistry. III. The role of exact exchange,” *J Chem Phys*, vol. 98, no. 7, pp. 5648–5652, Apr. 1993, doi: 10.1063/1.464913.

[49] C. Lee, W. Yang, and R. G. Parr, “Development of the Colle-Salvetti correlation-energy formula into a functional of the electron density,” *Phys Rev B*, vol. 37, no. 2, pp. 785–789, Jan. 1988, doi: 10.1103/PhysRevB.37.785.

[50] P. L. Polavarapu, “Ab initio vibrational Raman and Raman optical activity spectra,” *J Phys Chem*, vol. 94, no. 21, pp. 8106–8112, Oct. 1990, doi: 10.1021/j100384a024.

[51] A. Galano, N. A. Macías-Ruvalcaba, O. N. Medina Campos, and J. Pedraza-Chaverri, “Mechanism of the OH Radical Scavenging Activity of Nordihydroguaiaretic Acid: A

Combined Theoretical and Experimental Study," *J Phys Chem B*, vol. 114, no. 19, pp. 6625–6635, May 2010, doi: 10.1021/jp912001c.

[52] J. Ciubuc, K. Bennet, C. Qiu, M. Alonzo, W. Durrer, and F. Manciu, "Raman Computational and Experimental Studies of Dopamine Detection," *Biosensors (Basel)*, vol. 7, no. 4, p. 43, Sep. 2017, doi: 10.3390/bios7040043.

[53] J. L. Billinsky, M. R. Marcoux, and E. S. Krol, "Oxidation of the Lignan Nordihydroguaiaretic Acid," *Chem Res Toxicol*, vol. 20, no. 9, pp. 1352–1358, Sep. 2007, doi: 10.1021/tx700205j.

[54] P. Wagner and R. A. Lewis, "Interaction between activated nordihydroguaiaretic acid and deoxyribonucleic acid," *Biochem Pharmacol*, vol. 29, no. 24, pp. 3299–3306, Dec. 1980, doi: 10.1016/0006-2952(80)90307-X.

[55] V. Krishnakumar, G. Keresztury, T. Sundius, and R. Ramasamy, "Simulation of IR and Raman spectra based on scaled DFT force fields: a case study of 2-(methylthio)benzonitrile, with emphasis on band assignment," *J Mol Struct*, vol. 702, no. 1–3, pp. 9–21, Sep. 2004, doi: 10.1016/j.molstruc.2004.06.004.

[56] O. G. Taylor, J. S. Brzozowski, and K. A. Skelding, "Glioblastoma Multiforme: An Overview of Emerging Therapeutic Targets," *Front Oncol*, vol. 9, Sep. 2019, doi: 10.3389/fonc.2019.00963.

[57] J.-M. Lü, J. Nurko, S. M. Weakley, and J. Jiang, "Molecular mechanisms and clinical applications of nordihydroguaiaretic acid (NDGA) and its derivatives: An update," *Med.Sci.Monit.*, 2010.

[58] T. Seufferlein *et al.*, "Mechanisms of nordihydroguaiaretic acid-induced growth inhibition and apoptosis in human cancer cells," *Br J Cancer*, vol. 86, no. 7, pp. 1188–1196, Apr. 2002, doi: 10.1038/sj.bjc.6600186.

[59] Y. Sun, N. J. Giacalone, and B. Lu, "Terameprocol (Tetra-O-Methyl Nordihydroguaiaretic Acid), an Inhibitor of Sp1-Mediated Survivin Transcription, Induces Radiosensitization in Non-small Cell Lung Carcinoma," *Journal of Thoracic Oncology*, vol. 6, no. 1, pp. 8–14, Jan. 2011, doi: 10.1097/JTO.0b013e3181fa646a.

[60] B. L. Carlson, J. L. Pokorny, M. A. Schroeder, and J. N. Sarkaria, "Establishment, Maintenance, and In Vitro and In Vivo Applications of Primary Human Glioblastoma Multiforme (GBM) Xenograft Models for Translational Biology Studies and Drug Discovery," *Curr Protoc Pharmacol*, vol. 52, no. 1, Mar. 2011, doi: 10.1002/0471141755.ph1416s52.

[61] Y. Zhou *et al.*, "Human brain cancer studied by resonance Raman spectroscopy," *J Biomed Opt*, vol. 17, no. 11, p. 116021, Nov. 2012, doi: 10.1117/1.JBO.17.11.116021.

[62] F. Röhrig and A. Schulze, "The multifaceted roles of fatty acid synthesis in cancer," *Nat Rev Cancer*, vol. 16, no. 11, pp. 732–749, Nov. 2016, doi: 10.1038/nrc.2016.89.

[63] J. Long *et al.*, “Lipid metabolism and carcinogenesis, cancer development.,” *Am J Cancer Res*, vol. 8, no. 5, pp. 778–791, 2018, [Online]. Available: http://www.ncbi.nlm.nih.gov/pubmed/29888102

[64] G. Gueron *et al.*, “Game-changing restraint of Ros-damaged phenylalanine, upon tumor metastasis,” *Cell Death Dis*, vol. 9, no. 2, p. 140, Feb. 2018, doi: 10.1038/s41419-017-0147-8.

[65] S. B. Jones, *Sistematica Vegetal*. Mexico, 1988.

CURRICULUM VITA

Jose Guerrero was Born on December 22, 1992. The youngest son of Isela and Mario, he graduated from Eastwood High school, El Paso, Texas, in the summer of 2011. He entered El Paso Community College in fall 2013 to study physics. He was later transferred to The University of Texas at El Paso in the spring of 2015. During his last year of undergraduate, he did condense matter physics research under Dr. Vivian Incera, the chair of the physics department at the time. He received his bachelor's degree in Physics in the summer of 2018.

In the Fall of 2018, he was admitted to the M.S. graduate program in the Department of Physics at The University of Texas at El Paso. He performed his graduate research in the Optical Spectroscopy and Microscopy Laboratory under Dr. Felica Manciu. During his graduate studies, he was financially supported as a Teaching Assistant. Graduated in the spring of 2020 with his master's degree and received the "Academic and Research Excellence Graduate Student Physics Award".

He then later went to be accepted in the Environmental Science and Engineering PhD program and supported financially by the Graduate school. During his PhD studies, he remained in the Optical Spectroscopy and Microscopy Laboratory under Dr. Felica Manciu. He was awarded the Graduate Excellence Fellowship allowing him to further financially support his PhD education.